Craters of the Pluto-Charon system

Stuart J. Robbins [a,*], Kelsi N. Singer [a], Veronica J. Bray [b], Paul Schenk [c], Tod R. Lauer [d],
Harold A. Weaver [e], Kirby Runyon [e], William B. McKinnon [f], Ross A. Beyer [g,h], Simon Porter [a],
Oliver L. White [h], Jason D. Hofgartner [i], Amanda M. Zangari [a], Jeffrey M. Moore [h],
Leslie A. Young [a], John R. Spencer [a], Richard P. Binzel [j], Marc W. Buie [a], Bonnie J. Buratti [i],
Andrew F. Cheng [e], William M. Grundy [k], Ivan R. Linscott [l], Harold J. Reitsema [m],
Dennis C. Reuter [n], Mark R. Showalter [g,h], G. Len Tyler [l], Catherine B. Olkin [a],
Kimberly S. Ennico [h], S. Alan Stern [a], the New Horizons LORRI, MVIC Instrument Teams

[a] Southwest Research Institute, 1050 Walnut St., Suite 300, Boulder, CO 80302, United States
[b] Lunar and Planetary Laboratory, University of Arizona, Tucson, AZ, United States
[c] Lunar and Planetary Institute, Houston, TX, United States
[d] National Optical Astronomy Observatory, Tucson, AZ 85726, United States
[e] The Johns Hopkins University, Baltimore, MD, United States
[f] Washington University in St. Louis, St. Louis, MO, United States
[g] SETI Institute, 189 Bernardo Avenue, Suite 100, Mountain View CA 94043, United States
[h] NASA Ames Research Center, Moffett Field, CA 84043, United States
[i] NASA Jet Propulsion Laboratory, California Institute of Technology, Pasadena, CA, United States
[j] Massachusetts Institute of Technology, Cambridge, MA, United States
[k] Lowell Observatory, Flagstaff, AZ, United States
[l] Stanford University, Stanford, CA, United States
[m] Ball Aerospace, Boulder, CO, United States
[n] NASA Goddard Space Flight Center, Greenbelt, MD, United States

ARTICLE INFO

ABSTRACT

NASA's *New Horizons* flyby mission of the Pluto-Charon binary system and its four moons provided humanity with its first spacecraft-based look at a large Kuiper Belt Object beyond Triton. Excluding this system, multiple Kuiper Belt Objects (KBOs) have been observed for only 20 years from Earth, and the KBO size distribution is unconstrained except among the largest objects. Because small KBOs will remain beyond the capabilities of ground-based observatories for the foreseeable future, one of the best ways to constrain the small KBO population is to examine the craters they have made on the Pluto-Charon system. The first step to understanding the crater population is to map it. In this work, we describe the steps undertaken to produce a robust crater database of impact features on Pluto, Charon, and their two largest moons, Nix and Hydra. These include an examination of different types of images and image processing, and we present an analysis of variability among the crater mapping team, where crater diameters were found to average $\pm 10\%$ uncertainty across all sizes measured ($\sim$0.5–300 km). We also present a few basic analyses of the crater databases, finding that Pluto's craters' differential size-frequency distribution across the encounter hemisphere has a power-law slope of approximately -3.1 ± 0.1 over diameters $D \approx$ 15–200 km, and Charon's has a slope of -3.0 ± 0.2 over diameters $D \approx$ 10–120 km; it is significantly shallower on both bodies at smaller diameters. We also better quantify evidence of resurfacing evidenced by Pluto's craters in contrast with Charon's. With this work, we are also releasing our database of potential and probable impact craters: 5287 on Pluto, 2287 on Charon, 35 on Nix, and 6 on Hydra.

© 2016 Elsevier Inc. All rights reserved.

1. Introduction

NASA's *New Horizons* mission to the Pluto-Charon system is the first mission to explore the last of the classical planets and first to explore objects in the Kuiper Belt. The data gathered in July 2015 provided a first look beyond basic albedo maps

(Buie et al., 2010) at the largest known Kuiper Belt Object (KBO) and the largest binary planetary system known in the solar system. The system is embedded within the inner edge of the Kuiper Belt, so it is impacted by a distinct population of bodies that we cannot probe from the study of giant planets' moons, and current detection technology from Earth can only observe the largest KBOs. Because of this, the crater population of Pluto and Charon was predicted, modeled, and estimated (e.g., Bierhaus and Dones, 2015; Greenstreet et al., 2015) – but unknown – and any potential geologic activity could modify the recorded crater population formed by those impactors. Therefore, mapping the crater population of Pluto and Charon is an important probe into not only the impactor population, but also geologic processes occurring on both bodies. Crater population information (the size-frequency distribution (SFD)), morphologies observed, depth relative to diameters, and basic superposition relationships can all be used to inform researchers about exogenic and endogenic processes as well as basic chronology. The first step is to catalog those impact craters.

For past missions to new bodies, crater measurement and cataloging has almost always been the purview of whomever is trying to accomplish whatever science with them; i.e., there has rarely been a concerted effort by researchers dedicated to mapping impact craters to create a core dataset from which others would work. This has changed in recent years, especially with the *Dawn* mission to both (4) Vesta and (1) Ceres, wherein different teams within the mission worked to generate independent crater catalogs. Unfortunately, the different teams produced significantly different crater catalogs which led to what some in the sub-field have termed "The Vesta Controversy," wherein derived surface ages of features differ by over 1 billion years and the modeled impactor flux varies significantly (e.g., Marchi et al., 2012, 2013; Schmedemann et al., 2013, 2014; O'Brien et al., 2014; Schenk et al., 2015). At (1) Ceres, the teams still developed independent catalogs, but they have worked to reconcile differences, or at least to better understand what the differences are (Hiesinger, pers. comm., 2016).

With this in mind, as well as work demonstrating substantial variability among crater analysts (Gault, 1970; Robbins et al., 2014), crater analysts within the *New Horizons* Pluto Encounter Team decided *a priori* to develop independent crater lists and then combine and reconcile them for a final, consensus crater database for each body observed. This approach takes into account natural researcher variability and it presents a single, core database from which further work can be done.

Pulling as much information from the available data is a prime goal for any mission, but for several weeks after the flyby, only lossy compressed data were returned. There has not previously been a focused effort to understand the effects of image compression on mapping impact craters, though there have been efforts to understand image compression on planetary image data (e.g., Klaasen et al., 1997, 1999). Therefore, besides cataloging the impact craters, a secondary purpose of the work presented in this paper is to demonstrate the effects of some data manipulation techniques on the ability to map impact craters and the effects of the particular image compression scheme used by *New Horizons* on crater identification. This is discussed in detail in Section 2, and a guide between the PDS ID and Request ID (a more colloquial name, and found within the PDS header) for the images used for these comparisons is listed in Table 1.

Section 3 of this paper describes how a consensus crater database of Pluto, Charon, Nix, and Hydra was constructed and compiled and it discusses some of the variability among the researchers. Section 4 discusses properties of the consensus database and overviews what they show about the surfaces of these four bodies (for related work, see: Stern et al. (2015); Moore et al. (2016), and Weaver et al. (2016)). Finally, Section 5 discusses conclusions and implications not only for the crater populations of

Table 1

Translation key between image or image sequence request name used in planning *New Horizons* observations, compared with the LORRI and MVIC image names that are likely to be used in PDS releases. "Image #" refers to the same pointing but a multiple-image sequence, and "frame #" refers to the image within a sequence with different pointings.

Request ID	PDS Name	Pixel Scale (km/px)
NAV_C4_L1_CRIT_34_02	LOR_0298787064	30.1
NAV_C4_L1_CRIT_35_02	LOR_0298893474	19.8
NAV_C4_L1_CRIT_35_03	LOR_0298893754	19.7
NAV_C4_L1_CRIT_37_02	LOR_0298996974	12.7
P_LORRI_FULLFRAME (image 1)	LOR_0299124574	3.86
C_LORRI_FULLFRAME (image 1)	LOR_0299147641	2.33
C_LEISA_LORRI_1 (frame 2)	LOR_0299171335	0.707
P_LORRI_STEREO_MOSAIC (frame 8)	LOR_0299174905	0.381
C_LEISA_HIRES (frame 4)	LOR_0299175604	0.416
C_LEISA_HIRES (frame 7)	LOR_0299175721	0.408
P_MPan1	MP1_0299178832	0.495

each body, but also implications of this work that may help future mission planners and image analysts to focus on observations, data return, and data processing that can benefit rather than hinder surface feature analysis.

Important Note: This paper makes use of informal names. These names have not been approved by the International Astronomical Union, and they are used here only to facilitate communication.

2. Different methods of working with *New Horizons* image data

New Horizons returned some of its earliest, high-resolution science data that could be used for geomorphologic study as lossy-compressed. These data were used by the science team to try to derive early science results, and now, more than a year after the closest approach, and with the uncompressed data available, how those results may have been biased due to the lossy data can be analyzed. This is important to understand because flyby missions are significantly easier to engineer, and with their rich history, NASA and other space agencies will unquestionably have more in the future. Understanding biases in the data interpretation from early returns based on processing unique to *New Horizons* can help future teams to avoid those errors. This section examines different ways the image data were processed onboard the spacecraft and what biases occurred. Specifically, lossy vs lossless compression is examined. In Appendix A, we also discuss the effects of and supersampling with deconvolution once the data were on the ground which can assist future mission planners and data analysts.

New Horizons recorded approximately 60 Gb during its encounter with the Pluto-Charon system, but it was limited in its data rate of return to Earth (∼1300–2000 bps). Data compression algorithms can shrink the data volume while preserving the information so long as they are lossless (e.g., a series of 25 letter "A"s could be represented as 25A without losing information). Lossy compression can reduce the data volume further, but there is a loss of information when this is used (e.g., a series of 24 letter "A"s with 1 B in the middle, represented as 25A, preserves the length but loses the letter B). The significance of lossy versus lossless image compression on the ability to map impact craters is examined herein. This is an important investigation because, if the lossy compression used onboard *New Horizons* does not significantly affect the images, then future missions could take advantage of this to return their data faster to Earth and allow more bandwidth for other missions. However, if the lossy compression used by *New Horizons* significantly compromises the ability to interpret the data, then future missions could use a different scheme, or they could save time (and risk – the July 4, 2015 safe mode just 11 days before closest approach was due to compression taking too long) on the spacecraft by not compressing the data and save time on the Deep

Space Network in not returning a "browse" dataset of lossy images before returning lossless versions. While this may have limited applicability to future missions as on-board computers improve, it has significant implications for planning the extended mission by *New Horizons*.

Compression was also investigated in other missions, especially *Galileo* (e.g., Klaasen et al., 1999) due to the failure of its main antenna, but *Galileo* used a different image compression scheme that introduced different artifacts than *New Horizon*'s (in particular, an integer cosine transform versus a discrete cosine transform form of JPG compression). Qualitatively, authors on this paper who participated in *Galileo* science investigations have determined that the lossy compression used by *New Horizons* results in more severe artifacts and loss of data than compression used by *Galileo* (this is extraordinarily difficult to quantify). Additionally, *Galileo*'s software was rewritten while the spacecraft was in operation to experiment with different compression schemes, and *Galileo* was able to take repeat images of different targets at different solar phase angles due to its orbit around Jupiter (excepting its flyby of (951) Gaspra and (243) Ida). *New Horizons*' software was not rewritten in flight, there was no repeat imaging after flyby, and therefore it represents a different set of circumstances.

The data volume of each LORRI (LOng-Range Reconnaissance Imager (Cheng et al., 2008)) image is approximately 3 MB (24 Mb), and the data volume for each MVIC (Multi-spectral Visible Imaging Camera (Reuter et al., 2008)) panchromatic scan can be 100s MB, if both are compressed using the lossless algorithm onboard the spacecraft. When lossy compressed, the data volume for each LORRI image shrinks by $\approx 2\times$ and MVIC by $\approx 6.5\times$ (only one lossy compression setting is available). LORRI was the highest resolution dataset for all regions of both Pluto and Charon, and so only lossy versus lossless data results for LORRI were tested here. Specifically, the lossy-compressed images returned for Charon images were the last full-frame images at 2.3 km/px (where Charon's full disk fit within the LORRI frame within the uncertainties of its position) and two images from a high-resolution mosaic (0.41–0.42 km/px) with one image near the center at of the disk (high sun) and one at the terminator (low sun). The lossy images returned for Pluto were also the full-frame (3.9 km/px) and seven images from a 3×5 mosaic at 0.36–0.40 km/px that fall mostly across Sputnik Planitia. (See Table 1.)

New Horizons uses a JPG schema for lossy image compression (Mick et al., 2008). In brief, the image is divided into a grid of cells, each covering an 8×8 square of pixels. The intensities of the pixels in a given cell are represented by the coefficients of a discrete cosine transform (DCT) over its area. The compression is done by discarding coefficients of low significance based on a model of the image noise, signal level, and an overall desired level of data compression. In most scenes, the structural power in the image decreases steadily with increasing spatial frequency. As such, the first effect of JPG compression is likely to be some level of smoothing as the coefficients describing the finest features are discarded. In some cases, the block is reduced to a single constant intensity level. At the same time, sharp features of high contrast may still be preserved if they generate especially large amplitudes in the higher-frequency DCT components. An attractive feature of the DCT is that it makes it easier to preserve continuity across block boundaries; however, as the level of compression increases, this becomes progressively more difficult, and the images take on a "blocky" appearance – particularly at low signal levels, or where the scene lacks sharp or high-contrast features. Paradoxically, the blockiness introduces spurious high-frequency power (sharp edges between blocks) that can disrupt or confuse the recognition of real features in the image.

Practically speaking, the strong blocky pattern associated with heavy JPG compression means that any features observed as 8 pixels across (or multiples thereof) require skepticism, and very smooth features may only be a compression artifact. An additional problem with JPG compression is that if there is low signal within the image, the compression artifacts and removal of signal will be more severe – this is the case with Charon in contrast with Pluto, where the compression blocks were visually more obvious on the former because Charon has a lower albedo.

For this analysis, both full-frame images of Pluto and Charon (Fig. 1), an area of Sputnik Planitia on Pluto (Fig. 2), and a high sun and low sun area of Charon (Fig. 3) were examined.

Pluto and Charon full-frame: Fig. 1 illustrates the crater population mapped by Robbins from lossy and lossless images of the full encounter hemispheres of Pluto and Charon, separated by both high confidence craters and all craters (see explanation in Table 2). The crater SFDs are very different for each body; this is likely caused by the significant difference in crater preservation (Pluto's craters are more heavily modified than Charon's). The higher confidence crater counts on Pluto from the lossy image show not only a different SFD, but they also are significantly fewer in number (by $\approx 8\times$). The data based on the lossy image also show a marked deficit of craters at $D \approx 12$ px, or 1.5 JPG blocks. The "high" versus "all" confidence craters from the lossless image are similar in shape, which is reassuring for repeatability. On Charon, the results are completely different. There would appear to be a multiplication or division by 2 error between the datasets, but this is how the craters were mapped on the lossy image returned the day after encounter versus the lossless version returned in September. At issue is that many of Charon's craters have a dark ejecta interior to bright ejecta which was not obvious in the lossy images, and so the dark ejecta was marked initially as the impact crater rims. This assumption did not factor into the confidence, which is why the population regardless of "all" versus "high" confidence craters on Charon is the same.

Half-kilometer per pixel Sputnik Planitia, Pluto: Fig. 2 illustrates a region of the high albedo area informally called Sputnik Planitia shown in lossy, lossless, and lossless deconvolved versions. When this image was first downlinked the day after closest approach, several features were identified as possible impact craters. Once the lossless versions were returned many days later, these features were shown to be simple darker albedo deposits and not impact craters. The DCT created a ringing effect in albedo which was interpreted as a possible impact feature.

High and low phase half-kilometer per pixel Charon: Fig. 3 shows two images of Charon. These two images were the only ones of a 5-image sequence returned lossy-compressed three days after closest approach, and the whole sequence was returned lossless two months later. The relative darkness of Charon contributed to more severe JPG compression artifacts, rendering the high sun image almost useless for crater mapping in its lossy form. However, the low sun image, despite the JPG compression, showed numerous relatively clear impact craters. The high sun data in Fig. 3 demonstrate a significantly different crater population between the lossy and lossless versions, wherein Robbins identified a mere 12 craters at high confidence in the lossy version versus 258 at high confidence in the lossless version. In the right column are shown data for the low sun image which demonstrates remarkable similarity not only between Robbins' mapping on lossy and lossless images, Robbins' high confidence versus all craters, but also between Robbins and Singer (Singer only marked high-confidence craters in this case and did not mark craters crossing the terminator nor image edge that Robbins did). There are only two primary differences: (i) The small-diameter end between lossy and lossless yield different results (expected, considering that 3.2 km corresponds to 1 JPG block), and (ii) Singer in general identifies fewer potential crater features than Robbins, as noted in Robbins et al. (2014) and likely because Singer has a higher threshold for considering a feature to
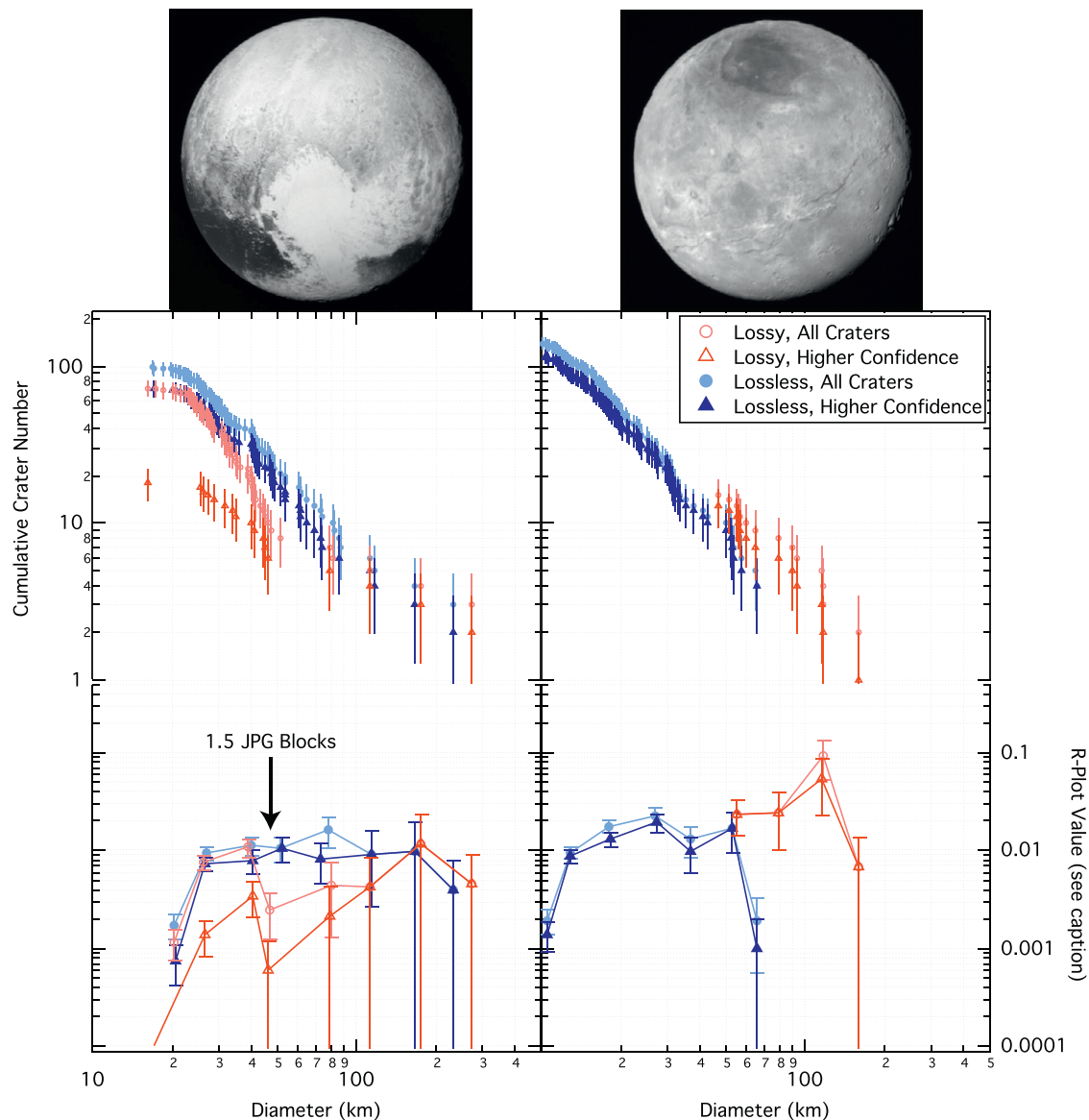
Fig. 1. Comparison of craters mapped on lossy and lossless versions of the last full-frame images of Pluto and Charon (LOR_0299124574, LOR_0299147641, respectively). Pluto data are shown in the left column, and Charon data are shown in the right column. Only Robbins' data are shown (other researchers did not do this comparison). "Higher Confidence" refers to craters with a subjective confidence of 3, 4, or 5 (see Table 2). The approximate completeness limit is 25 km (left) and 15 km (right). The top row shows the lossless images, the middle row shows a cumulative ranked list-style size-frequency distribution (crater diameter on the abscissa, and number in a sorted diameter list on the ordinate axis), and bottom row is a standard R-plot (Crater Analysis Techniques Working Group, 1979); note that the R-plot requires an area estimate, for which a half-sphere was used, but this over-estimates the actual mappable area so these values are artificially low. Cumulative crater number is not normalized per surface area. Uncertainty on the ordinate axis is SQRT(*N*) Poisson uncertainty.

be an impact crater, and Robbins a lower threshold. However, the population (i.e., the shape of the SFD) is similar between Robbins and Singer (a Kolmogorov-Smirnov test has a *P*-value = 0.88, where $P \leq 0.05$ indicates the null hypothesis that they are the same can be rejected).

From these comparisons, the lossy compression used by *New Horizons* can introduce significant biases and artifacts when trying to map impact craters, especially when one does not know *a priori* basic crater morphology on the body (e.g., Charon's craters' dark inner ejecta) and when the craters are heavily modified. It can also "create" impact craters because JPG compression is inherently "ringy" due to the DCT. However, there was one case (low sun Charon) that, despite the low signal-to-noise, and despite the JPG artifacts, the lossy vs lossless comparison showed that the image was reliable for crater mapping. This set of conclusions is important not only for future missions and downlink planning, but

also it is a warning for mission teams that desire to release results from crater mapping derived from lossy-compressed images. It also should serve as a caution for researchers who may try to gather early science results by using lossy compressed versions of lossy compressed images that are disseminated as press releases.

3. Constructing a consensus crater database

3.1. Mechanics of construction

In this section, the methods used to construct crater databases for bodies in the Pluto-Charon system are described. The approach has been informed by Robbins et al. (2014) which quantified, for the first time in a peer-reviewed work, the random and systematic variation in crater mapping by independent crater analysts using independent techniques. It has been a generally
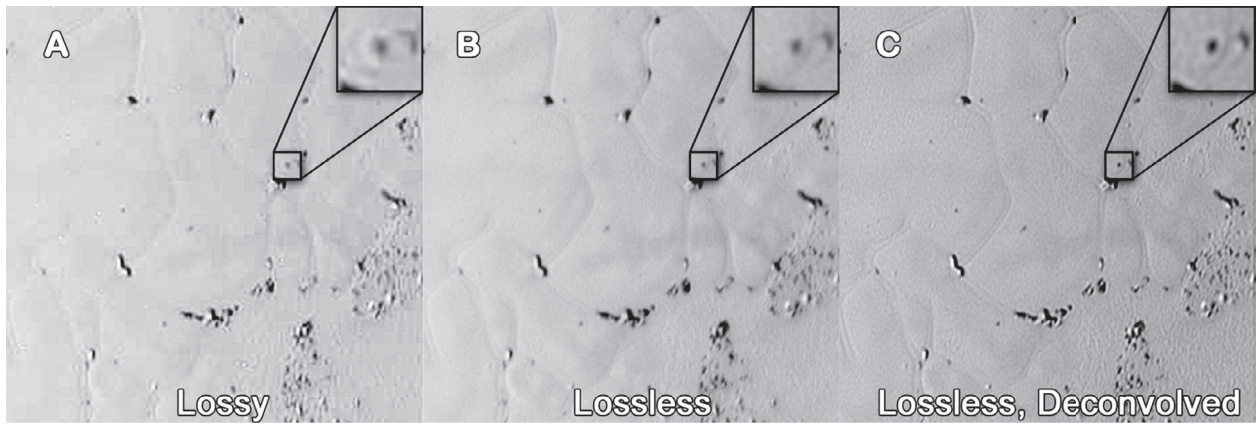
Fig. 2. Comparison of LORRI image LOR_0299174905 downlinked (A) with lossy compression, (B) with lossless compression, and (C) the lossless version deconvolved. Each has an inset of the same feature, expanded to 300%, in the upper-right corner (native scale is 0.38 km/px). These show how both compression and deconvolution can affect high-frequency albedo patterns to create the albedo pattern – the illusion – of an impact crater.
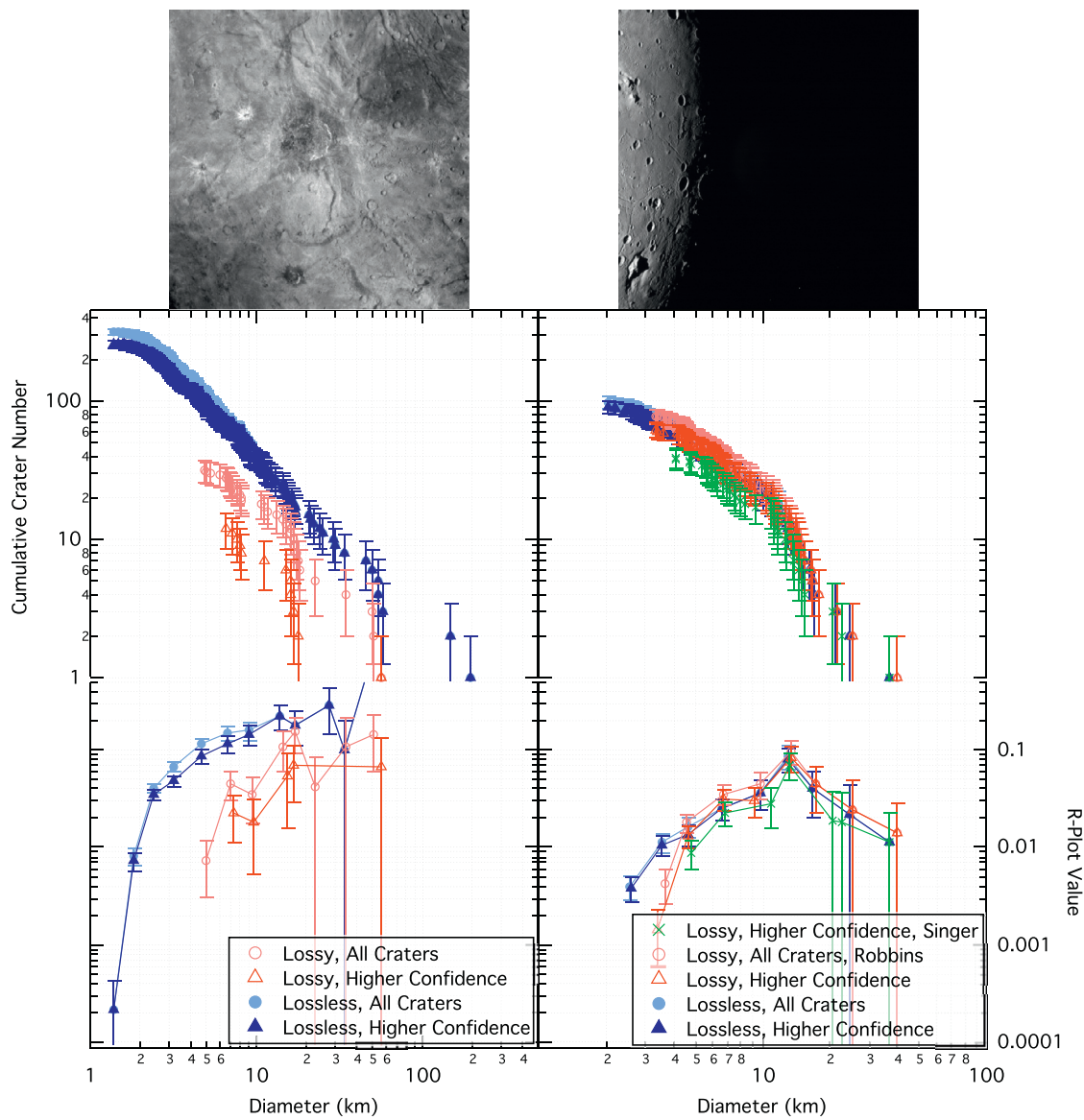

Fig. 3. Similar to Fig. 1 in data format and layout (including no normalization for the cumulative plot), but for two images of Charon. Left column is data from LOR_0299175604, and right column is data from LOR_0299175721, both images are unprojected; approximate surface areas are 300,000 km² and 69,700 km², respectively. Right column contains lossy data from Robbins and Singer; Singer only mapped high-confidence craters for this exercise. The approximate completeness limit is 3 km in both.

Table 2

Description of subjective confidence level assigned to craters by different researchers in this effort. All confidence levels were normalized to Robbins' 1–5 scale for the final catalog, where the individuals' ranking description (left-most column) is placed into the row to which it corresponds under Robbins' system.

Description	Robbins	Singer	Bray	Runyon	Weaver
Certain	5	1	*only*	*only*	Likely
Likely	4	2			
Possible ("50/50")	3	3			Possible
Probably not	2	4			
Interesting circular feature, but deemed not a likely crater	1	5			

Table 3

List of persons who contributed data to this crater mapping effort and what image(s) and/or image product(s) were used.

Person	Data
Robbins	All returned images of Pluto, Charon, Nix, and Hydra with multiple image processing techniques applied, for any images for which craters were visible (from approximately 4 days before encounter through encounter).
Singer	Full-disk mosaics of Pluto and Charon, high-resolution LORRI swaths of Pluto and Charon, MVIC scans of Pluto and Charon. All higher resolution images of Nix and Hydra.
Bray	Mosaic of Pluto.
Weaver	All images of Nix and Hydra.
Runyon	LORRI high-resolution images of Cthulhu region of Pluto.

unspoken phenomenon that different crater analysts will map craters differently; in fact, a single analyst can rarely duplicate their data exactly. Because of this, a goal in this work was to be as redundant as possible and to use multiple measurements from different people and/or different images from which to build a consensus database. Table 3 lists the persons and image set(s) they used that contributed to the final databases presented in this paper (note that the databases are *not* stored as supplemental material on the *Icarus* website, they are in an independent archive with USGS / NASA PDS and we may have made additions or revisions after the publication of this research paper).

After all measurements were made, there were tens of thousands of candidate crater markings, but most were duplicates (by design). A fully manual approach to combining these was not feasible, so an automated-assisted method was used. In early February 2016 when this was done, the control networks for both Pluto and Charon had offsets of 10 s km in many locations (larger than most craters), so the automated code often had difficulty distinguishing similarly sized craters that were within ∼3 crater radii of each other (control networks refine spacecraft pointing information to better align projected images). This offset existed for MVIC to LORRI registration and between some of the LORRI sequences. Therefore, every marking and possible cluster was manually checked and corrected as needed.

The automated code used is a customized version of the DBSCAN algorithm (Density-Based Spatial Clustering of Applications with Noise), originally developed by Ester et al. (1996) and first modified for use in clustering craters in Robbins et al. (2014). DBSCAN provides two key features that are important for this application. First, it is a hard clustering code which means that individual markings can only belong to one cluster (one final crater), or to none (a cluster with 1 member). Second, is has very few *a priori* inputs, making it more objective: (a) a "reachability" parameter and (b) the minimum number of points in a group required to be considered a valid cluster. Reachability is how cluster members are found, where a point is considered "reachable" by another point if it is within a certain distance of it or other members of the cluster to which it may belong.

The code was modified in Robbins et al. (2014) to incorporate a diameter-dependent scaling of distance that manifest as a second reachability parameter dependent solely on diameter. This means that, for example, two 20-km-diameter craters with centers 30 km away from each other would not be considered reachable and hence members of different clusters, but two 200-km-diameter craters with centers 30 km away would be considered the same feature. Requiring both reachability parameters means that if a crater was reachable by another based on location, it also needed to be reachable based on diameter. This allows two overlapping craters – i.e., a small crater superposed on a larger crater – to be separated that under a normal DBSCAN code would be grouped into one feature.

The input crater data were location $\{x, y\}$ and diameter D in addition to the confidence c. Both Robbins and Singer – the two primary crater mappers in this work – assigned a subjective confidence to each crater they marked that denoted the likelihood that the feature was really an impact crater; Weaver did the same for Nix and Hydra (see Table 2). The other two analysts, Bray and Runyon, only marked features they were highly confident were impact craters, and so those features were assigned a 100% confidence. The data output for each cluster of markings are: (a) mean $\bar{x}$ with standard deviation, δx; (b) mean $\bar{y}$ with standard deviation, δy; (c) mean $\bar{D}$ with standard deviation, δD; (d) number of points N in that cluster; and (e) mean of the confidence for the craters that went into that cluster, $\bar{c}$. (These averages and standard deviations are recalculated after validation (see next paragraph) and again after the control networks were finalized.) Additional details of this code can be found in Appendix C of Robbins et al. (2014). For the small satellites Nix and Hydra, clustering was fully manual due to the small numbers of features involved and lack of a coordinate system.

Subsequent to the automated code's output and manual correction of that output, there were approximately 2500 final craters on Charon and 5600 on Pluto; these represent all clusters (i.e., from *all* confidence levels for any marked feature from any returned image) that could be mapped on these bodies given all imagery returned from *New Horizons* of Pluto and Charon with diameters ≳20 px. No final clusters were rejected based on low confidence at this stage. Next, each final crater was re-examined and a revised confidence was attached based on the latest data, discussion between Robbins and Singer, and rejection of false positives; this process results in the final numbers listed in Section 4 (e.g., in low-resolution images, a feature might have been uncertain, lowering its overall confidence when averaged with high-resolution images, so in this re-evaluation the confidence would be increased). This confidence only represents whether the feature is real, and it does not reflect the confidence of its diameter or location.

Fig. 4 illustrates the fraction of craters in a given confidence range versus crater diameter for Pluto and Charon. This diagram clearly demonstrates that the team was more confident in mapping craters on more Charonian terrains than on Pluto. This was because Charon's landscape was more familiar with respect to other
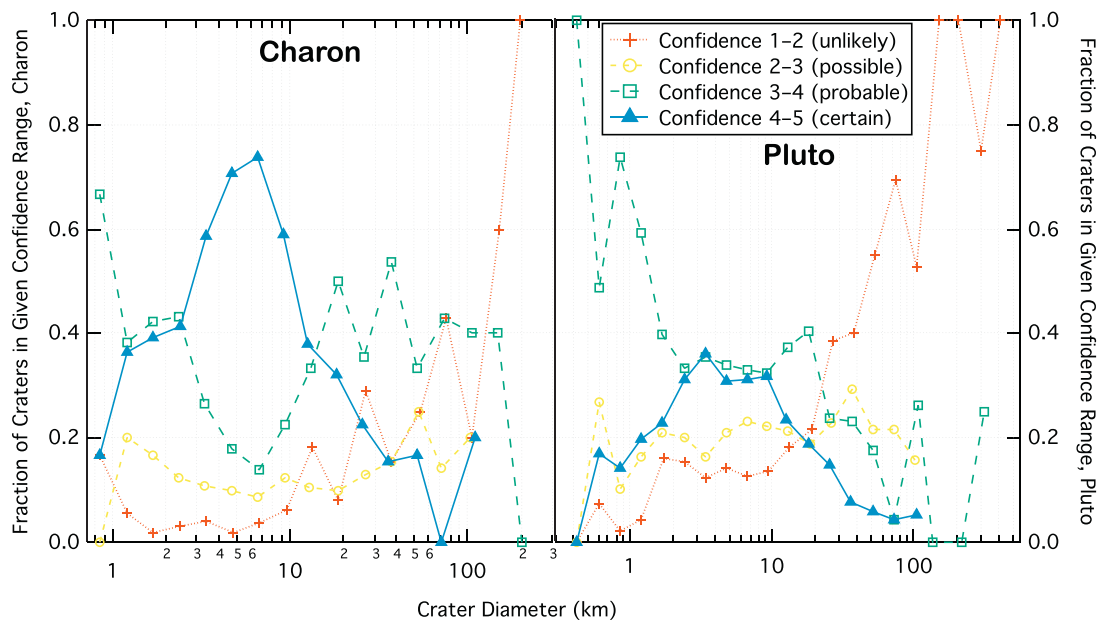
Fig. 4. Confidence of the final (duplicate markings merged) crater catalogs for Pluto and Charon as a function of diameter. Ranges are inclusive of the lower number, up to but not including the upper number (except for 4–5). Diameter axis for Charon is 0.8–300 km, and diameter axis for Pluto is 0.3–400 km. This shows, for example, that for craters $D \approx 10$ km, 35% of the Plutonian impact craters had a confidence c of $3 \leq c < 4$ (probable), whereas at $D \approx 100$ km, fully ≈ 50–70% of the Plutonian impact craters had a confidence level of $1 \leq c < 2$ (unlikely to be a crater, but worth noting as a possible feature). See discussion in Section 3.2.

solar system bodies; Vulcan Planum on Charon was particularly well exposed, well lit, and had less endogenic crater degradation; and Pluto's surface is significantly more modified by geologic and other processes that made crater identification more difficult. Overall, $\approx 88\%$ of the craters in the Charon catalog have a confidence ≥ 3, and $\approx 76\%$ of craters in the Pluto catalog have a confidence ≥ 3. This is diameter-independent except for the largest craters which encompass non-encounter hemisphere markings, such that, for craters $D \gtrsim 50$ km, the percentage drops to ≈ 50–60% for Charon and ≈ 10–30% for Pluto.

This confidence column is recommended to be used in three potential ways: First, for researchers who would like to use this catalog without their own verification, it is recommended that the catalog be clipped at a confidence at least ≥ 3 (on what many of the results in subsequent sections are based), or potentially ≥ 4 or even 5. This most conservative clip is intended for researchers who only want to work with absolutely unambiguous impact craters, exclusively on the encounter hemisphere of Pluto and Charon. A second method to use this confidence is as a check for researchers who do their own crater counts and use this catalog as a reference. An independent assessment of the crater population by that researcher should certainly not miss any confidence = 5 impacts, almost no confidence = 4, and go down from there. Alternatively, the independent researcher may take all confidence ≥ 4 craters without checking, and then manually examine each < 4 for possible inclusion in their own work. The authors of this work recognize that crater identification is not a wholly objective process (see next subsection) and as such, the authors request any person who finds error within the catalog to contact the corresponding author (Robbins) to make corrections.

3.2. Repeatability of crater identifications, diameter measurements

With a final catalog created by merging multiple markings from one individual and individual markings from other researchers, the natural variability in the crater identifications can be examined. Because different iterations of the coordinate system for each body were used at different times by the individuals involved, only

two aspects of variability were studied: How many craters were identified in a given region, and the measured diameter varied for individual craters.

3.2.1. Crater identification replicability

Past work has primarily focused on comparing one crater analyst relative to another on the same image to minimize many independent variables that are inherent in using multiple kinds of images (e.g., lighting, resolution, slant angle, smear). In this work, that scenario was rare but more "real-world" because different people generally used different image products (Table 3). In this sub-section, Nix impact craters mapped by three individuals on the same LORRI image and MVIC scan are compared; and Pluto's larger craters mapped by Robbins on all available images, Singer on parts of the closest approach MVIC scan along with the full-disk LORRI mosaic, and Bray on the composite map rendered in November 2015 are compared.

Nix: Two images of Nix were examined under different image processing that are described in detail in Section 4.3. In brief, these were a high-sun LORRI image and low-sun MVIC scan and independently marked impact craters. In the high-sun, Robbins identified 11 (9 at confidence ≥ 3), Singer identified 5 (5 at high confidence), and Weaver identified 7 (5 at high confidence) craters. All high confidence craters marked by Weaver were also identified by Singer, and Robbins also identified those as high confidence. The additional craters Robbins identified may be expected since identifying craters in low resolution images on irregularly shaped bodies enhance the challenges associated with crater identification. Due to the particularly small numbers, SFDs are not useful comparisons. However, for the MVIC scan, Robbins identified 23 craters (19 at confidence ≥ 3), Singer identified 14 (8 at high confidence), and Weaver identified 24 (16 at high confidence). Both Weaver and Robbins identified all craters that Singer did, and all but two of Weaver's overlapped with Robbins'. The *population* (SFD slope) of the higher confidence craters mapped by Robbins, Singer, and Weaver all are similar (via K-S test) for diameters $D \geq 6$ km, which corresponds to ≈ 13 px. Not only that, but the number of craters is also within 1σ uncertainty. For smaller diameters, Singer

found a shallower slope that is due to an incomplete sampling relative to Robbins and Weaver – or over-interpretation by Robbins and Weaver – while Robbins and Weaver have identical populations (via K-S test) for diameters of craters as small as ≈2 px. This comparison should not be misconstrued to imply that Nix craters as small as 2 px are fully represented, but rather this comparison shows that two independent analysts can come remarkably close to duplicating each others results completely independently and with independent techniques.

Pluto: For Pluto, crater populations based on significantly different datasets were compared. To control for areas that different analysts did not map, the comparison focused on the area 10–50°N, 70–150° E (North of Cthulhu, West of Sputnik Planitia). In this area, Robbins identified 2104 impact craters (using images down to 0.08 km/px), Singer identified 519 impact craters (using images down to 0.82 km/px over the full area), and Bray identified 476 impact craters (using a global mosaic). Of these, 1773 of Robbins' and 445 of Singer' had confidence ≥3 (Bray only identified high confidence craters). (Note that the extreme mismatch in number is due to Robbins using >10× higher resolution images in some areas.) When compared in a cumulative SFD, the populations each found were similar for craters $D \gtrsim 8$ km (again based on a K-S test). The number of $D \geq 8$ km craters each found was 497, 333, and 280 (Robbins, Singer, Bray, respectively). Robbins' and Bray's SFD shape were more similar for craters $D \gtrsim 5$ km than to Singer's, and they found 824 and 430 craters.

Two observations were made from this comparison. First, as identified before, there can be a significant variation in the *number* of impact craters mapped by different crater analysts. In this case, a factor of 1.8–1.9× in number of craters mapped is still less than the spread for an average lunar highlands image in Robbins et al. (2014), and some of this variation could also be attributed to Robbins' use of better pixel scale imagery than the global mosaic that Bray used. However, the second observation underscores that most analysts identify the same *population* (SFD shape), as quantified in a K-S test, at least for diameters larger than what would be considered the onset of incomplete counts due to finite pixel scales. While the former observation should raise a factor of uncertainty in crater identification, the latter should be reassuring when assessing the size-frequency distribution of crater observations.

3.2.2. Crater diameter replicability

As with understanding the variability in number of craters found and the shape of the crater size-frequency distribution, very few researchers have published on the replicability of the crater diameters that are mapped. In Robbins et al. (2014), the researchers found a diameter-independent spread of approximately ±7%·D in crater diameters between researchers, regardless of crater preservation state except for the sharpest of impact craters. That study gave every researcher the same two images of the lunar surface. In this work, up to four individuals mapped the same features on different images spanning almost two orders of magnitude in pixel scale. *A priori*, one would expect the scatter in diameters to be larger.

Fig. 5 illustrates the diameter variability found on Pluto and Charon. For every crater that was marked at least twice, the 1σ spread from the mean diameter, normalized by the mean diameter, is shown on the vertical axis versus mean diameter on the horizontal axis (i.e., the relative uncertainty in the diameter is shown versus the crater diameter). To better visualize the average, these were binned to show the mean and standard deviation of a log-normal distribution of the data points within each diameter bin range. These data show that the scatter in mapped crater diameter as a fraction of crater diameter is diameter-independent, and as predicted, the scatter is larger than in the Robbins et al. (2014) study. For both Pluto and Charon, the scatter is ≈11%•D
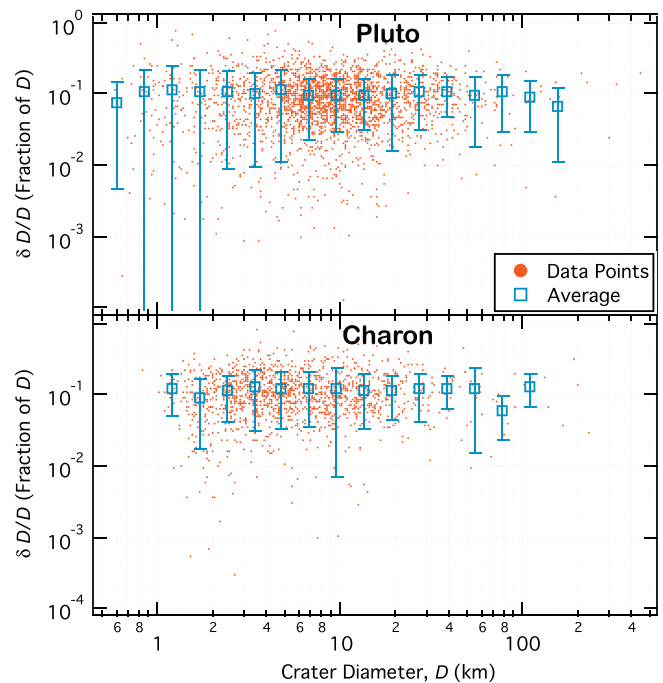

Fig. 5. Scatter points are impact craters that were marked at least twice, regardless of confidence level, and boxes with uncertainty lines show average and standard deviation of the values within multiplicative $2^{1/2}D$ bins. Vertical axis shows the standard deviation in crater diameter measurements for all markings that were members of that final cluster, divided by the mean crater diameter. Top plot is Pluto, bottom is Charon, and all axes cover the same ranges.

(Charon: ±12%·D with a 1σ spread averaging ±8%; Pluto: ±10%·D with a 1σ spread averaging ±9%).

This is a natural variation in mapping crater diameters from this type of mission, and as such, it is an uncertainty that should be carried through to all other analyses, such as scaling laws and understanding the impactor population. However, since the analyses presented in the remainder of this manuscript are based on the population of numerous impact craters, and standard analysis techniques in the field have no method to factor these in (Crater Analysis Techniques Working Group, 1979), it is not propagated for the Pluto and Charon analyses (but is in Nix and Hydra, where N is small).

4. The consensus impact crater population within the Pluto-Charon system

The primary goal in this work was to create a crater database for Pluto, Charon, Nix, and Hydra that includes all potential craters and can be used by researchers for science investigations. This effort should not be misconstrued to have produced global, uniform databases because of the severe pixel scale and lighting variations across each body. For reference in subsequent sections, Figs. 6 and 7 present maps showing the sun angle, pixel scale, and emission angle for Pluto and Charon, respectively, of the best images for geomorphologic mapping. Inset in each are histograms showing the fractional coverage of each body at each incidence angle and pixel scale.

4.1. Pluto

4.1.1. Global distributions

From 12,759 candidate crater-like features on Pluto (including all confidence levels and duplicate markings), the final crater catalog has 5287 features that are possible impact craters (duplicate features merged and including all confidence levels) and
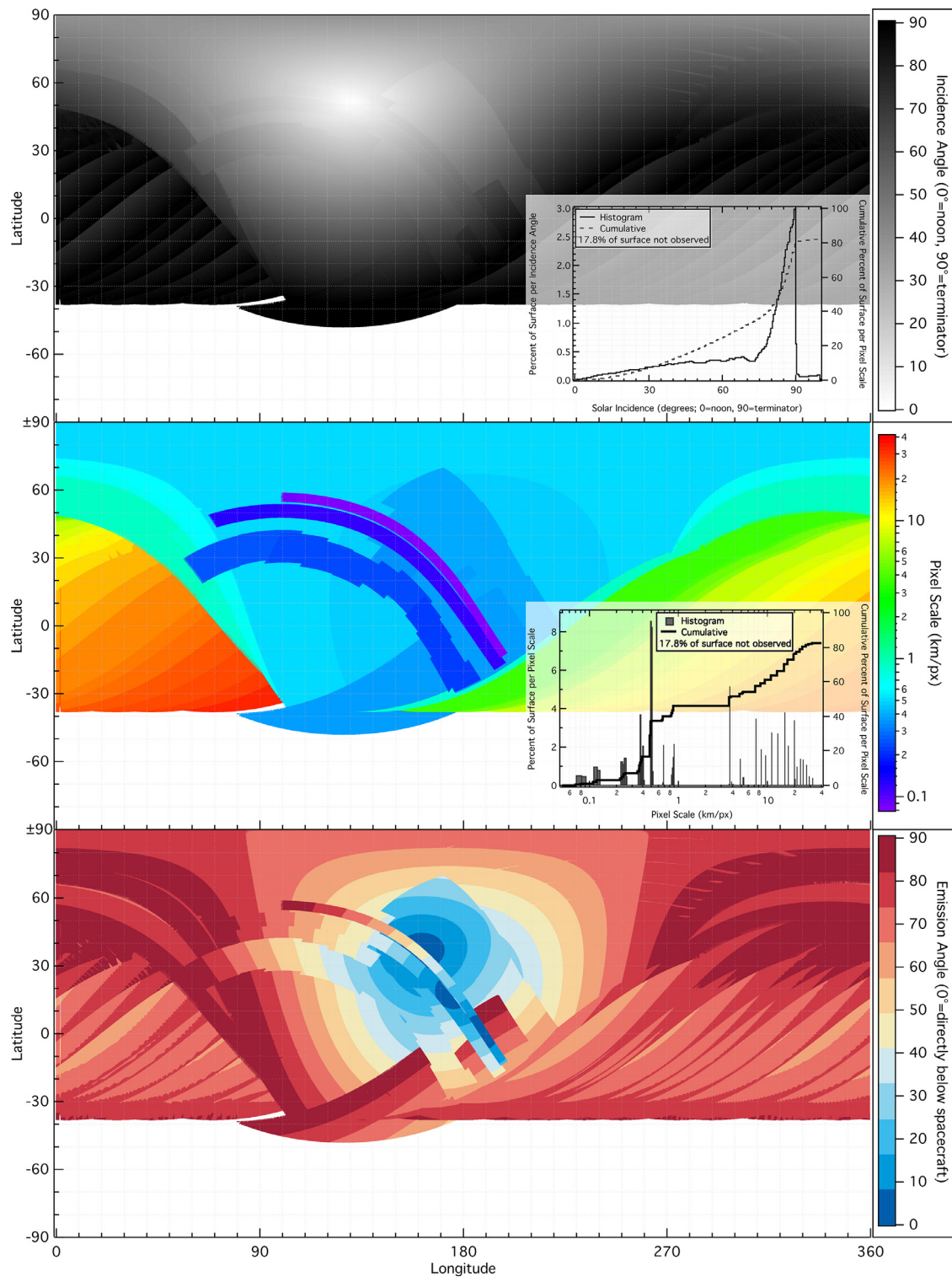
Fig. 6. Top— This map shows the solar incidence angle of the best quality images for geomorphologic studies returned from the *New Horizons* spacecraft by February 2016. Incidence angle ranges from 0° (noon sun) to 110° (sun beyond the terminator due to haze lighting). Middle— This map shows the pixel scale of those same images. Pixel scale ranges from 0.08 to 31.41 km/px. Bottom— This map shows the emission angle of those same images from 0° (directly below the spacecraft) to 90° (limb). Inset Top— Histogram shows the percentage of the surface of Pluto at a given solar incidence angle. Left axis corresponds to the histogram which is binned in 0.5° intervals and is the solid line. Right axis corresponds to the dashed line which is a cumulative histogram. Approximately 17.8% of the body was not imaged, for it was in permanent shadow during the *New Horizons* flyby. Inset Middle— Histogram shows the percentage of the surface of Pluto at the best pixel scales. Left axis corresponds to the histogram which is binned in 0.01 km/px intervals and is the shaded bars to zero. Right axis corresponds to the thick black line which is a cumulative histogram. Bottom axis is logarithmic.
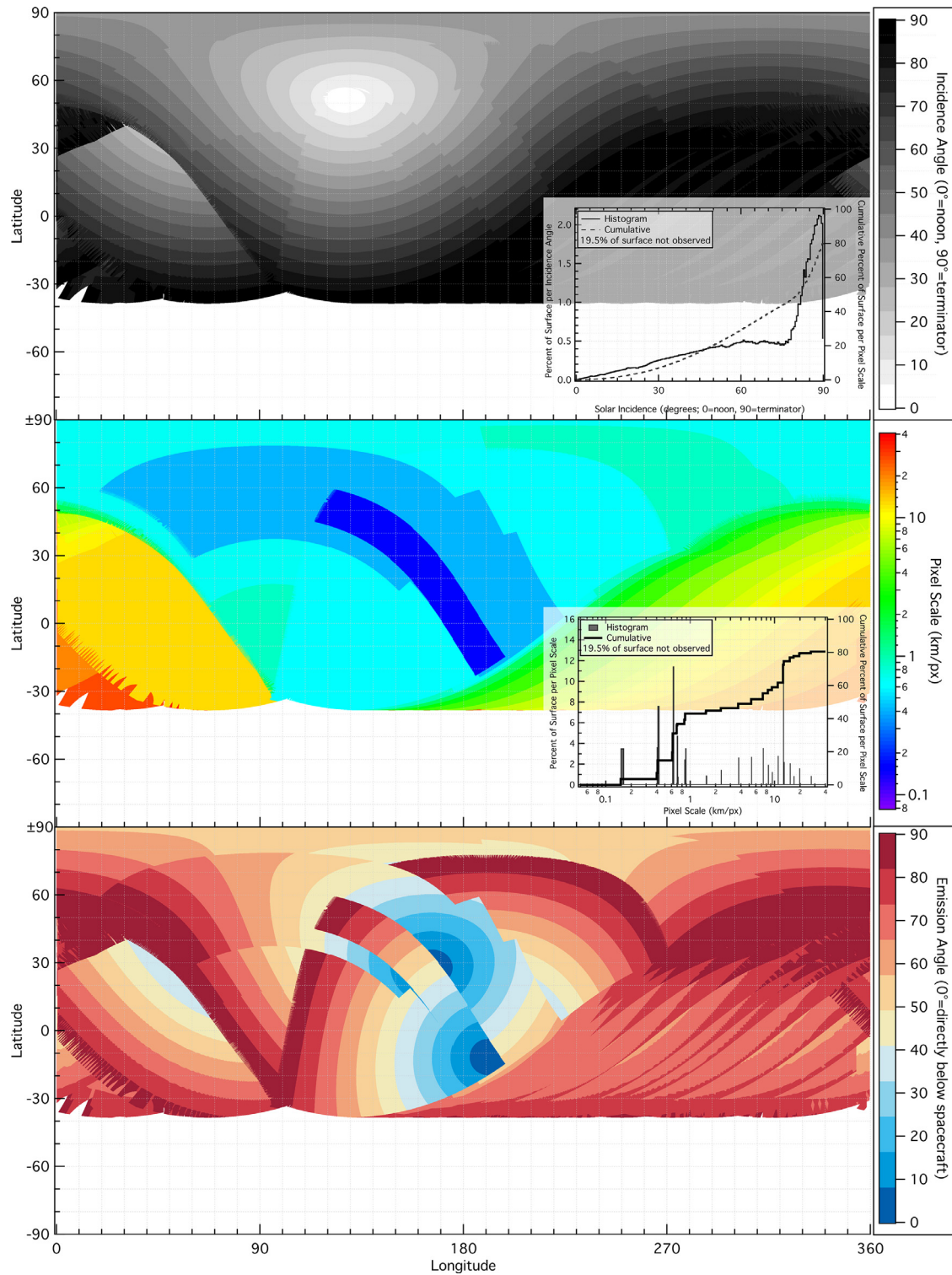
Fig. 7. Same as Fig. 6, but for Charon. Pixel scale ranges from 0.15 to 31.39 km/px and incidence angle cuts off at 90° because there was no atmosphere to assist in nightside viewing. Approximately 19.5% of the body was not imaged.

4030 features that are probable impact craters (duplicate features merged and confidence ≥ 3). Fig. 8 shows the results of this catalog, mapped across the body, in three different ways. The top panel shows a "completeness" map which assumes that a crater incremental SFD should increase from large to small diameters at least over the diameter range that could be measured. Under that assumption, if, going from large to small diameters, the SFD decreases (fewer craters are found at smaller diameters), that means

the ability to map these features has failed as opposed to a real deficit in small craters. If that is true, then the top panel maps out on Pluto to what diameter the crater catalog is complete for a given location. (In practice, the code searches near the maximum SFD frequency value to avoid small number variations at large diameters.) This map is smoothed by a radius of 207 km (10° at the equator) to increase the number statistics and present a smoother visualization, and for this top panel, craters of all confidence
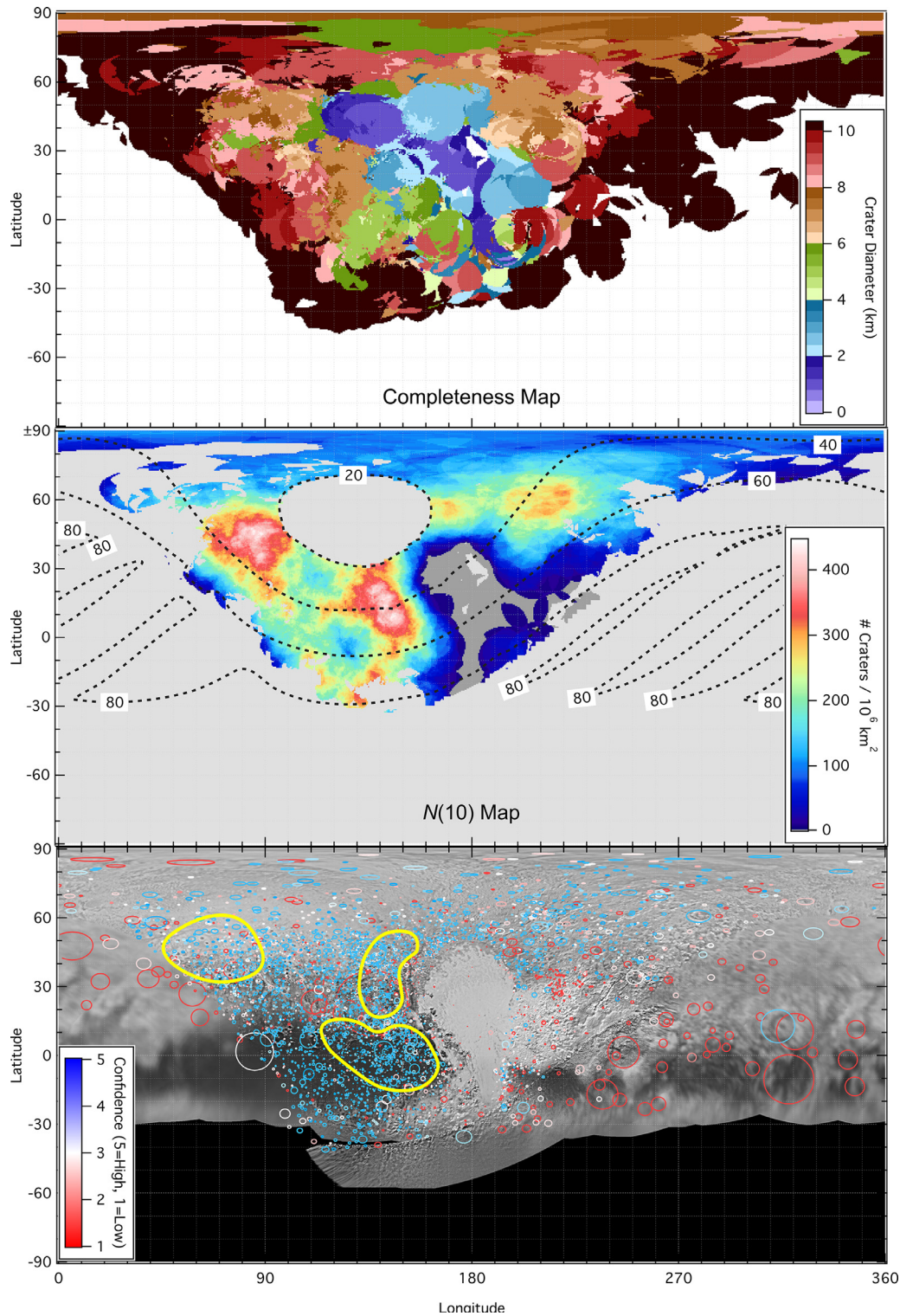
Fig. 8. Maps illustrating the crater distribution on Pluto where the top and bottom are all craters, and the middle plot are craters with confidence ≥ 3. Top and Middle (Kernel Density Plots)— The body was binned in 0.5° latitude by 0.5° longitude. All craters within a radius of 207 km (10° at the equator) from the center of each bin, regardless of confidence, were extracted from the final database. Top ("Completeness Map")— The craters within the given radius for each bin were plotted as incremental SFDs. The SFDs were read from large to small diameters, and the diameter bin where the next-smallest had fewer craters was saved as the value for that 0.5° by 0.5° position. This transition diameter is color-coded per the color scale legend, and those with diameters > 10 km are colored dark red. This completeness map is fully a function of the sun angle and pixel scale of available images (Fig. 6) except for the Sputnik Planitia area in the middle of the graph which had no discernable superposed impact craters. Middle ("N(10) Map")— Since much of the encounter hemisphere is complete for craters $D \geq 10$ km, the number of $D \geq 10$ km craters at each grid point was saved and scaled to the surface area of the radius of interest. Only craters with a confidence of ≥ 3 (Table 2) were included in this middle panel, and it has been masked such that only areas which are "complete" for $D \geq 10$ km are shown. It has also been masked such that areas with incidence $i < 20°$ and $i > 85°$ have been removed, as have areas viewed only at pixel scales > 1 km/px. Dark grey areas are where there were *no* impact craters with confidence ≥ 3 and $D \geq 10$ km within the 207 km radius of interest. Bottom— Approximate rim traces of every crater in the database color-coded based on confidence (Table 2). These are overlaid on the latest basemap. Areas outlined in yellow are areas from which craters were selected for the SFDs in Fig. 9.

levels were included. What it shows is that, as one would expect given Fig. 6, completeness is to smaller diameters where there is better image coverage, but also that small craters ($D \sim 0.5$ km at ~ 0.08 km/px) could still be discerned even when the sun was close to overhead, even though this is almost certainly an under-representation in the near-noon sun areas.

The middle panel of Fig. 8 shows a similarly smoothed $N(10)$ crater density map for Pluto, given that much of the surface over the encounter hemisphere has reasonably complete crater counts for $D \geq 10$ km; the craters for this panel are only those with a final confidence ≥ 3. It has been masked (light grey) where the solar illumination is $< 20°$ or $> 85°$, and/or where the best images are >1 km/px; dark grey indicates no craters on terrain that was not masked. The bottom panel of Fig. 8 shows idealized circle outlines tracing the rims of all craters in this catalog, color-coded by confidence (see Table 2). From these maps, several observations can be made, all using confidence ≥ 3 impact craters:

a. The terrain west of Sputnik Planitia (Venera, Voyager, and Viking Terras) has the largest $N(10)$ crater density observed on Pluto.
b. Sputnik Planitia is the only large, single geologic area of Pluto observed at ≤ 5 km/px that has no discernable superposed impact craters.
c. Areas southeast, south, and southwest of Sputnik Planitia have substantially lower crater densities, and therefore younger ages, than areas west and northwest of the Planitia. These areas included some of the best imagery for crater mapping and therefore the deficit of observed craters is real.
d. Tombaugh Regio's right and left sides (where the left, or west, side is Sputnik Planitia) are distinct in age as evidenced by their different $N(10)$ densities.
e. The north polar region, north of $\sim 80°$N, has a younger surface age based on $N(6)$ than the dense region west of Sputnik Planitia; the spatial density of craters $D \geq 6$ km is approximately 5–6× less around the north pole.
f. Even when larger craters are used for $N(D)$ (e.g., $N(20)$), the dark Cthulhu Regio (west of Sputnik Planitia) has fewer mappable impact craters (that size and larger) than the terrae mentioned above (but more than the areas south, southeast, and immediately southwest of Sputnik Planitia). It is possible that this area is so mantled by dark material that it has rendered many craters unmappable, or it underwent an erosive event that removed many larger (< 10 s km) craters.

4.1.2. Size-frequency distributions

A differential power-law slope fit to confidence ≥ 3 craters across the encounter hemisphere of Pluto for $D > 15$ km yields -3.08 ± 0.09 (all slopes were fit using Maximum Likelihood for a truncated power law (Aban et al., 2006) and uncertainty is 1σ). However, regional crater SFDs can be examined to determine whether any given area of Pluto has experienced significantly different resurfacing than others, beyond the points raised above and given the caveat of the sun angle shown in Fig. 6. Geologic mapping of Pluto is in progress (White et al., 2016), but since a full encounter hemisphere map is not yet available, three different sub-regions of the body that had similar $N(10)$ densities were examined (approximate outlines in Fig. 8): A portion of Cthulhu Regio (dark area west of Sputnik Planitia, selected area east of Edgeworth crater that was also covered by the highest resolution MVIC scan), a portion of Viking Terra (area immediately west of Sputnik Planitia), and Vega Terra (westernmost area with high-resolution coverage, separated from other areas by Piri Rupes to the east). Important Note– These regions are not necessarily singular geologic units; rather, they are regions defined in preliminary, informal nomenclature maps (Stern et al., 2015; Moore et al., 2016).
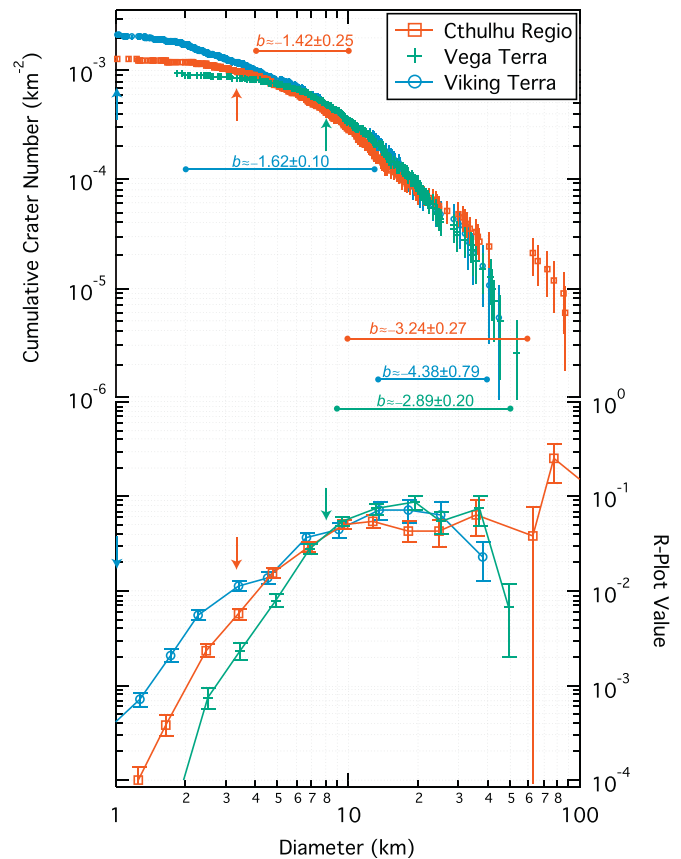

Fig. 9. Similar to Fig. 1 in graph format and layout. Data are SFDs for three regions of Pluto's surface from the consensus database; approximate surface areas are 398,000 km² for the Vega Terra sub-region, 188,000 km² for the Viking Terra sub-region, and 337,000 km² for the Cthulhu Regio sub-region. Data are only for craters with a confidence ≥ 3. Slope labels were fit to a differential SFD, not to cumulative. Small arrows indicate approximate completeness diameter.

The crater counts are shown in Fig. 9. Completeness is estimated as $D \approx 4.3$ km for this sub-region of Cthulhu, $D \approx 1.0$ km for Viking Terra, and $D \approx 6$–10 km for Vega Terra (range for Vega Terra due to uncertainty in whether the slope difference in $D \approx 6$–10 km range is real or due to inability to identify craters). Examination of Fig. 9 shows only one significant difference in the three regions that is likely to be real. The main obvious difference is that the slopes for craters $D \lesssim 6$ km in the three regions are different, but given both lighting effects and limited high-resolution LORRI image coverage (Fig. 6), these differences are likely crater detection artifacts rather than real. The other primary difference in the SFDs is for craters $D \approx 15$ km and $D > 60$ km in Cthulhu Regio, which is likely to be real (see next paragraph).

When fitting the differential SFD for the sub-region of Cthulhu Regio, over the range $D = 4$–10 km, the slope is a shallow -1.42 ± 0.25; over the diameter range $D = 10$–60 km, the slope is a steep -3.24 ± 0.27. When fitting a slope to the differential SFD for the sub-region of Viking Terra, over the range $D = 2$–15 km, the slope is similar Cthulhu's small craters, -1.62 ± 0.10; over the diameter range $D = 15$–40 km, the slope is steeper at -4.38 ± 0.79. When fitting a slope to the differential SFD for the sub-region of Vega Terra, over the range $D = 9$–50 km, the slope is -2.89 ± 0.20. Two main observations can be made from these. First, the larger diameter populations of each region are relatively steep compared with smaller diameters, and though they vary by ≈ 1.5, they have overlapping uncertainties. Also, Vega Terra's shallower slope might be attributable to lighting rather than a distinct resurfacing or crater population, but further investigation is needed. The second observation is that both Cthulhu and Viking have distinctly shal-

lower slopes at smaller diameters, and because of the crater diameters at which these are observed relative to the pixel scale of the images on which they were mapped, this is very likely to be real. This indicates probable resurfacing rather than a bend in the impactor population because the shallowness of the slope is significantly more than on Charon (see Section 4.2.2).

4.2. Charon

4.2.1. Global distributions

From 8266 candidate crater features on Charon (including all confidence levels and duplicate markings), the final crater catalog has 2287 features that are possible impact craters (duplicate features merged and including all confidence levels) and 2022 features that are probable impact craters (duplicate features merged and confidence ≥ 3). Fig. 10 shows the results of this catalog, mapped across the body, in three different ways. These are identical in construction to Fig. 8 and explained in Section 4.1.1. What Fig. 10 shows is that, as one would expect given Fig. 7 and as found for Pluto, completeness is to smaller diameters where there is better image coverage, but also that small craters ($D \sim 1$ km at ~ 0.16 km/px) could still be discerned even when the sun was close to overhead, even though this is almost certainly an under-representation in the near-noon sun areas.

The middle panel of Fig. 10 shows a smoothed $N(10)$ crater density map for Charon; the craters for this panel are only those with a final confidence ≥ 3 (the radius of interest used was the same for Pluto, corresponding to approximately 20° at Charon's equator compared with 10° at Pluto's). While Fig. 10a suggests that much of the encounter hemisphere of Charon may be complete for craters $D \geq 5$ km (potentially due to the large MVIC scans relative to the body size on Charon versus Pluto), for direct comparisons with Figs. 8a and 10b was restricted to $N(10)$. The bottom panel of Fig. 10 shows idealized circle outlines tracing the rims of all craters in this catalog, color-coded by confidence (see Table 2). From these maps, several observations can be made, all using confidence ≥ 3 impact craters:

(a) The encounter hemisphere of Charon is split by a prominent diagonal tectonic belt with at least 10 km vertical relief. Besides splitting the body geologically, it also splits the body in terms of craters that are easy to observe (south of it, on Vulcan Planum) versus those which are more difficult to observe and identifications are based more on albedo (north of it, on Oz Terra). This lighting geometry heavily biases results, despite the ability based on albedo to map very small (but likely only younger) impact features where there is high resolution image coverage.

(b) Vulcan Planum (the region south of the tectonic belt) has approximately the same number of observed impact craters as Oz Terra, for $N(10)$ counts with the ~ 200-km smoothing radius (Figs. 10 and 11). There is, however, a diagonal "corridor" of lower crater-density terrain spanning from approximately 0°E 40°N to 20°E 0°N. Given the significantly larger crater densities on either side of this "corridor" in both Oz Terra and Vulcan Planum, and the similar lighting conditions and different pixel scales, this is likely a real feature. This is likely because there exist a larger number of tectonic features throughout this area (Beyer et al., 2017, this volume).

(c) Vulcan Planum's crater population is far from saturated, for there are large regions of smooth plains (Moore et al., 2016). That Pluto and Charon would not be saturated with craters at any diameter was predicted by Bierhaus and Dones (2015) and models in Greenstreet et al. (2015).

(d) The area north of the tectonic belt has more $D \gtrsim 50$ km impact craters than Vulcan Planum (24 $D \geq 50$ km craters

with confidence ≥ 3 are in the catalog, 4 on Vulcan Planum (432,000 km^2), 14 in Oz Terra (910,000 km^2), and the remainder on the non-encounter hemisphere) – also reported in Moore et al. (2016). With point (b) above, a possible interpretation of the sequence of events is that Oz Terra has an older formation age (in agreement with Moore et al., 2016), Vulcan Planum formed subsequently which removed pre-existing craters $D \lesssim 50$ km (or perhaps Oz Terra and Vulcan Planum were resurfaced in the distant past to remove those craters), and then Oz Terra was resurfaced again to remove $D \lesssim 30$ km craters while Vulcan Planum was not. This would preserve the largest craters in Oz Terra while preserving ~ 10 s km craters in Vulcan Planum and removing many in the northern hemisphere. However, this is a somewhat *ad hoc* scenario, and it is possible that the $D \sim 10$ s km crater deficit in Oz Terra is simply due to lighting effects.

(e) The $N(5)$ crater density throughout Vulcan Planum (not shown in Fig. 10) varies significantly (~ 500–850 craters·10^6 km^{-2}), despite the region having relatively uniform pixel scale, incidence angle, and emission angle coverage (Fig. 7); ergo, this variation is likely real. The lower crater densities generally align with "patterned ground" and dense networks of further tectonic structures in the area (Beyer et al., 2017, this volume; Robbins et al., 2016).

(f) The north polar area has very few observable impact craters. This could be an artifact of lighting given its very dark, red mantling. It could also be a real feature, indicating that the north pole of Charon was resurfaced much more recently than other observed areas.

4.2.2. Size-frequency distributions

A differential power-law slope fit to confidence ≥ 3 craters across the encounter hemisphere of Charon $D > 10$ km yields -2.98 ± 0.16, which is the same to within 0.4σ of Pluto's average SFD slope. Individual regions' SFDs can be examined to determine whether any given area of Charon has experienced significantly different resurfacing than others, beyond the points raised above and given the caveats of Fig. 7. Geologic mapping of Charon is underway (Robbins et al., 2016), but since encounter hemisphere maps are not yet available, one sub-region each of two different areas of the body were compared. Both of these were imaged during the LORRI ride-along of the closest-approach MVIC scan at approximately 0.16 km/px, and both are at similar lighting geometries (approximate outlines in Fig. 10). The crater counts are shown in Fig. 11.

Within their uncertainty, these populations appear almost identical except that the Vulcan Planum population is more complete to smaller diameters due to better lighting conditions – completeness is estimated as $D \approx 2.7$ km for Oz Terra and ≈ 2.2 km for Vulcan Planum. When fitting a slope to the differential SFD for Vulcan Planum over the range $D = 2$–13 km, the slope is -2.47 ± 0.15; over the diameter range 13–30 km, the slope is significantly steeper, -8.39 ± 2.70 (while this is incredibly steep and has a large error bar, we are confident enough to say that it *is* steeper in this diameter range but the exact slope value is subject to large uncertainty). For the sub-region of Oz Terra, over $D = 3$–20 km, the slope is -2.38 ± 0.19. Therefore, within the uncertainty, these regions have similar slopes. Combined with the Pluto data, especially given the favorable lighting in Vulcan Planum, this change in slope at $D \approx 10$ km in large regions on both bodies is suggestive of an exogenic factor rather than endogenic, though as stated above, the more drastic change at $D \approx 10$ km on Pluto almost certainly has a significant endogenic component.
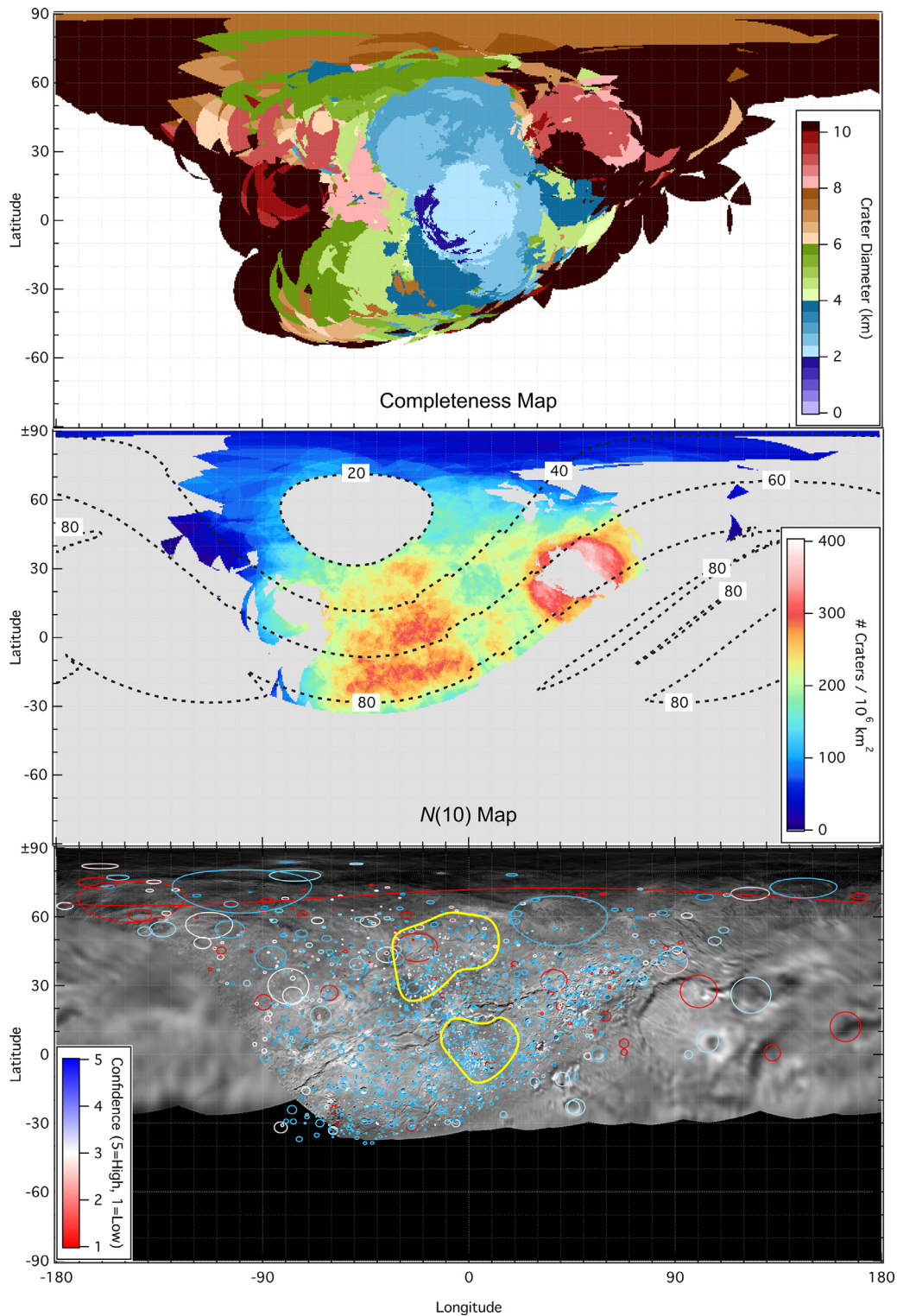
Fig. 10. Maps illustrating the crater distribution on Charon. See Fig. 8 caption for explanation, though the smoothing radius for the top and middle panels equates to ≈20° at Charon's equator due to the smaller body size.

4.3. Nix and Hydra

The two larger of the four small moons of the Pluto-Charon binary system were imaged at enough resolution to identify impact craters: Nix, which was relatively close to the craft during the system fly-through, and Hydra which was farther away (Showalter and Hamilton, 2015; Weaver et al., 2016; Porter et al., 2016, this

volume). In particular, there were three observations of Nix that were suitable for mapping impact craters, one taken with LORRI at 0.774 km/px and low solar incidence (8.4°), a second LORRI at 0.302 km/px and low solar incidence (9.5°), and one taken with MVIC in panchromatic mode at 0.449 km/px and high solar incidence (85.9°). These images were taken at a range as close as 61 Mm. There was one sequence of well resolved Hydra images,
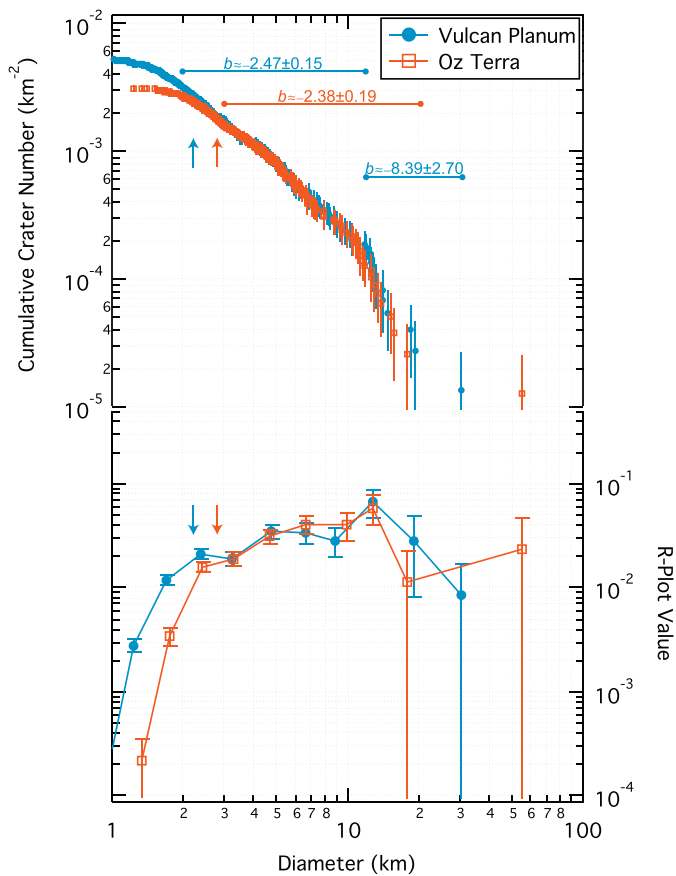
Fig. 11. Similar to Fig. 1 in data format and layout. Data are SFDs for two regions of Charon's surface from the consensus database, both in the closest-approach LORRI image sequence at ≈0.16 km/px; approximate surface areas are 74,300 km² for the Vulcan Planum sub-region and 78,600 km² for the Oz Terra sub-region. Data are only for craters with a confidence ≥ 3. Slope labels were fit to a differential SFD, not to cumulative.

where two pointings of two images each contained the moon. The range to Hydra was 227.5–229.4 Mm and its phase was approximately 34°. The pixel scale was 1.137 and 1.147 km/px for each pair, and there was a small rotation of the moon in the 1.5 minutes between the pair.

For these bodies, Robbins, Singer, and Weaver mapped impact craters. Because these bodies are irregular, these impact craters were not mapped onto an established cartographic grid. Instead, craters were measured in pixel space. For image processing:

- Nix at 0.774 km/px: This was a sequence of 6 images due to position uncertainty wherein Nix fortuitously appeared in a corner covered by 4 images. These were combined and sub-sampled by a factor of 4, and Robbins used the combined version for mapping craters. He also used a version of this that had been sharpened.
- Nix at 0.302 km/px: Used in its original state by Robbins (twice) and Singer, and it was used after sharpening by Weaver.
- Nix at 0.449 km/px: Used in its original state by Robbins (twice) and Singer, and it was used in a sub-sampled (2x) and sharpened state by Robbins and Weaver.
- Hydra at ≈1.14 km/px: Robbins used averaged subsampled versions with and without sharpening of each pair, and Singer and Weaver used an averaged subsampled version of one pair.
- Note: While Singer examined all images except 0.774 km/px Nix in their raw state, sharpened/deconvolved versions were also examined to inform markings (see Appendix A).

Table 4
Comparison of calculated $N(5, 10)$ densities for different surfaces and bodies in this work. $N(1)$ densities are discussed in the text for Nix but are not shown here because all $N(1)$ densities needed to be extrapolated in this work.

Body / Region	$N(5)$ km^{-2}	$N(10)$ km^{-2}
Pluto, Densest	0.00033	0.00026
Charon, Densest	0.00057	0.00044
Nix	0.0046 ± 0.0022	0.0027 ± 0.0014
Nix, Scaled[a]	0.0022 ± 0.0010	0.0013 ± 0.0007
Hydra		0.0024 ± 0.0023
Hydra, Scaled[a]		0.0011 ± 0.0011

[a] Using gravity scaling of 2.1 for non-porous ice (Holsapple, 1993).

4.3.1. Nix craters

Due to the relatively few craters, these were matched manually in two phases. First, all of Robbins' marks were matched across the different iterations and image processing to create a master list of his craters. Only craters identified at least twice were considered real. Second, Robbins' final crater list for each image was matched with Singer's and Weaver's. If Singer and/or Weaver identified a crater that Robbins only marked once, Robbins' marking was included in the average as an exception to the rule that Robbins needed to observe the feature at least twice. Average crater diameters, the standard deviation, number of analysts who observed the feature, and average confidence given, per image, formed the final crater list for Nix.

The results are in Fig. 12 for the 0.302 km/px LORRI image and the MVIC image. Three different datasets are in each panel, indicating all craters observed (by 1 or more persons), craters that were observed by at least 2 persons, and craters that had a high confidence (4 or 5 on Robbins' normalized scale; this threshold was used instead of the ≥ 3 confidence for Pluto and Charon mainly because both Singer and Weaver gave a more binary "likely" or "possible" confidence for these two moons). With small numbers, it is difficult to estimate which sub-set best represents the true crater population of Nix, and each researcher will need to use their own judgment. In this section and the next on Hydra, ranges are given based on bounds set by using just high confidence craters or those marked by ≥ 2 analysts (there were only 3 out of 42 cases (7%) where high-confidence craters from one analyst were not marked by either of the others).

The area normalization was significantly more complicated and prone to uncertainty for Nix than Pluto and Charon. Using results from Porter et al., 2016, (this volume), the surface area of an ellipsoid with major axes $(50 \times 35 \times 33) \pm 3$ km was calculated, giving a range of 4100–5580 km². The fraction of the surface observed in each image was then calculated. For the 0.302 km/px LORRI image, it was estimated that craters over $40 \pm 5\%$ of the surface could be mapped, giving a range of 1440–2510 km² for the counting surface; for the MVIC image, $25 \pm 5\%$ of the surface is the estimate, giving a range 820–1680 km². Crater counts were normalized to the average of each surface area and the uncertainty in crater density in each case was increased by 40% beyond the standard SQRT(N) Poisson counting uncertainty to reflect this. The uncertainty in crater diameter (standard deviation from the average diameter) is also displayed on each datapoint in the top row of Fig. 12.

From these, standard spatial densities can be estimated (and compared in Table 4). Because of the high sun of the LORRI image, it does represent a complete count, and this statement is supported by the significantly larger crater spatial density from the MVIC image. Therefore, using the MVIC image: $N(10) \approx 0.0027 \pm 0.0014$ km^{-2}, $N(5) \approx 0.0046 \pm 0.0022$ km^{-2}, and $N(1) \approx 0.016 \pm 0.006$ km^{-2} (extrapolated). Weaver et al. (2016) estimated a

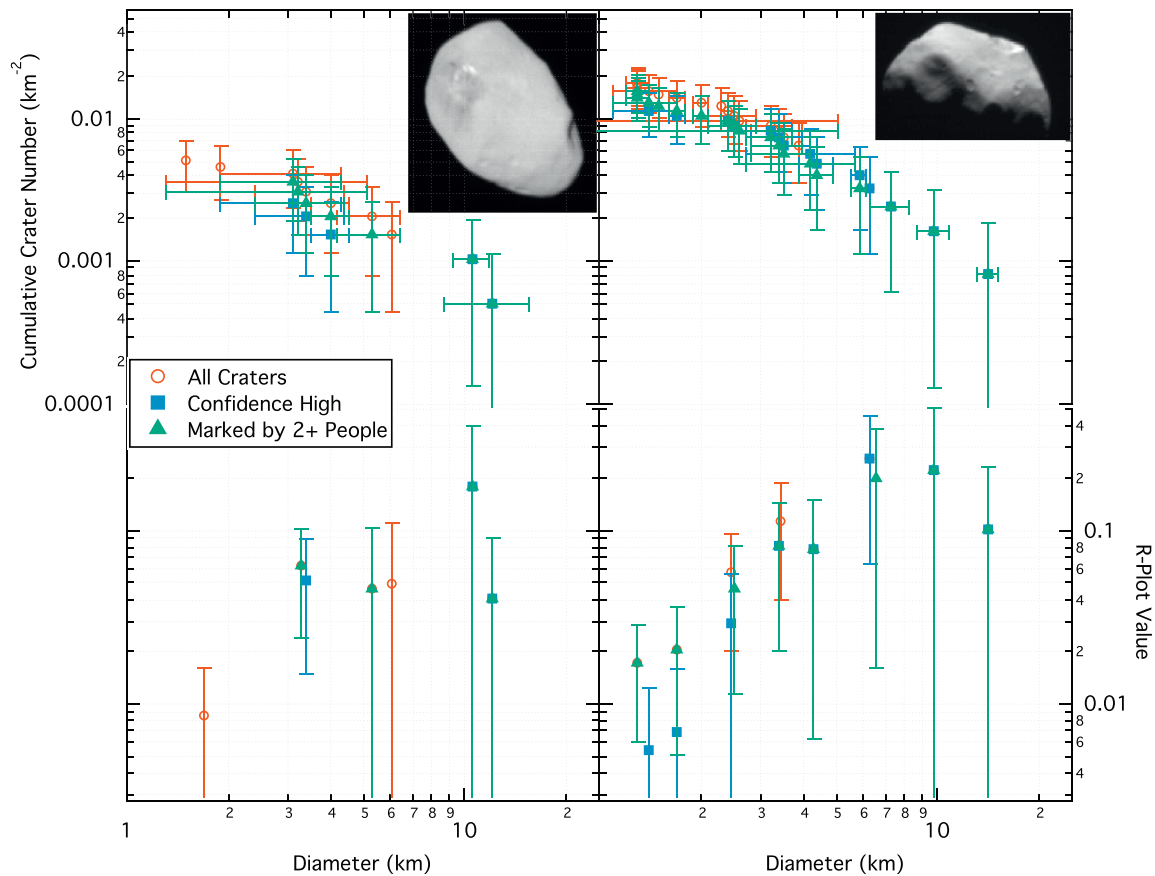**Fig. 12.** Crater population of Nix based on the best LORRI image and MVIC scan (0.304 and 0.449 km/px, respectively). Left column shows the LORRI image-based data, taken at approximately 10° phase, and right column shows MVIC image-based data, taken at approximately 86° phase. Images are shown in the upper right of each column. Uncertainty on each crater diameter is based on the standard deviation in diameter measurements by analysts, and uncertainty on the spatial density is SQRT(N) Poisson uncertainty multiplied by 1.3 to factor in uncertainty of the surface area mapped.

surface age of order 4 Ga for Nix and Hydra based on the "knee" model in Greenstreet et al. (2015). A gravity-scaling factor (e.g., Holsapple, 1993) of 2.1–2.6× (range is for endmember material parameters of non-porous ice to porous regolith) can be applied to scale the sizes of Nix and Hydra craters to those of Pluto for comparison (discussed in more detail in Weaver et al., 2016). The $N(10)$ density for the densest areas of Pluto is ≈0.00026 km^{-2}, such that when Nix is scaled down by 2.6, its $N(10)$ density is ~4× that of Pluto. This indicates a significantly older surface age. Similarly, Charon's $N(10)$ maximum is ≈0.00044 km^{-2}, so Nix's $N(10)$ is ~2× denser (Charon's densest $N(5)$≈0.00057 km^{-2}, so Nix's $N(5)$ is ~3× denser). This implies that no matter how ancient different portions of both Pluto and Charon appear (that were observed), they still have experienced resurfacing since the formation of the small satellites.

4.3.2. Hydra craters

With Hydra on the opposite side of the system from the spacecraft, and the range between *New Horizons* and Hydra almost 4 times as far as to Nix, very few impact craters are distinguishable on the body despite its larger size. Nineteen features were marked between all three analysts which reduce to 5 craters that were marked at least twice, and SFDs are shown in Fig. 13. For Hydra, the size of the body is more uncertain, where Porter et al., 2016, (this volume) found a triaxial ellipse ($65 \times 45 \times 25$) ± 10 km. This yields a surface area of 3730–9360 km^2, and ≈35 ± 5% of the surface could be viewed. Therefore, the cumulative crater counts were normalized to an area of 2430 km; ±50% was multiplied into the

SQRT(N) uncertainties. Only $N(10) \approx 0.0024 \pm 0.0023$ km^{-2} could be estimated. The approximate surface age is of order ~4 Ga (Weaver et al., 2016). To within the ability to measure with *New Horizons* data, the surface ages of Nix and Hydra are both ancient, dating close to the formation of the system, and they are approximately the same.

5. Discussion

In this work, we have presented the basic results of a catalog of all possible and probable impact craters for Pluto, Charon, Nix, and Hydra from the *New Horizons* mission to the Pluto-Charon system (Section 4). While we illustrated the catalog and discuss basic crater densities and populations, we also discussed the methodology of how the catalog was constructed by merging numerous individuals' crater lists (Section 3). This work also demonstrated the effects of the specific, unique compression algorithm affected early data interpretations and how different types of image processing can alternatively help or hurt the crater mapping process (Section 2, Appendix A). From this work, we can enumerate 8 main conclusions:

1. Crater identification *must* be informed by geologic context. Craters appear different across the solar system, and while Charon's craters appeared mostly familiar, identifying probable craters on the heavily modified surface of Pluto was not trivial, and features such as possible suncups or volcanic structures can resemble impact structures. This was a contributing factor to
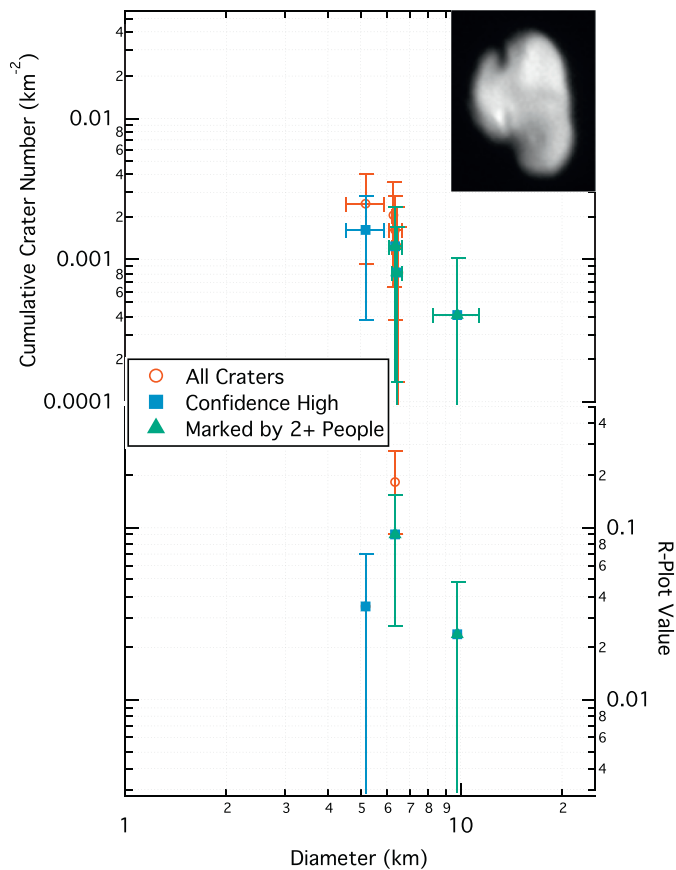
Fig. 13. Crater population of Hydra based on the best LORRI sequence (1.137 and 1.147 km/px image pairs). The images were taken at approximately 34° phase and one example is shown in the upper right. Uncertainty on each crater diameter is based on the standard deviation in diameter measurements by analysts, and uncertainty on the spatial density is SQRT(N) Poisson uncertainty multiplied by 1.5 to factor in uncertainty of the surface area mapped.

5. The crater population of Charon that we can observe is generally ancient (∼4 Ga (Moore et al., 2016)), but some crater density differences exist across its surface.

6. The differential SFD slope averaged over the encounter hemisphere of Pluto is –3.08 ± 0.09 for $D > 15$ km, but in selected areas we measured over diameters $D \approx$ 10–50 km, the SFD has a weighted average slope of –3.1 ± 0.2, while shallower diameters ≈2–10 km have a weighted average slope –1.6 ± 0.1. Similarly, craters over the encounter hemisphere for Charon have a differential SFD slope –2.98 ± 0.16 for $D > 10$ km. These overall slopes for Pluto and Charon are the same to within 0.4σ, as one would expect if similar impactor populations had struck and if resurfacing affecting large crater diameters over the majority of the mapped areas is similar. At smaller diameters ($D \lesssim$ 10–15 km), Pluto's SFD is significantly shallower than Charon's (weighted mean for Charon is –2.4 ± 0.1), and this is likely attributable to more active erosion on Pluto. This is supported by visual inspection of Pluto's surface which shows evidence for much more active geologic processes than Charon's (e.g., Stern et al., 2015; Moore et al., 2016).

7. Nix and Hydra have large crater densities, approximately 3 × the densest areas of Charon assuming 2.6 × gravity scaling (so ∼8 × without scaling), indicating an ancient origin (Weaver et al., 2016). This is despite Hydra's rapid rotation rate (which could be interpreted as a recent origin), but given this crater-based model age, the rapid rotation rate is likely due to spin-up from large impacts (Porter et al., 2016, this volume).

8. In the Appendix, we demonstrate the use of sub-pixel dithering to counter the effects of aliasing in an under-sampled camera. The use of supersampling and deconvolving the result allowed us to reliably map impact craters as small as $D \gtrsim 5$ px, validated for the full encounter hemisphere of Charon where this was used (Fig. 14). If confirmed for other missions' cameras, this methodology could allow reliable detection of craters (and other features) to practically half the size we could map before, simply by taking two images slightly separated and applying these image processing techniques. This also has implications for mission planning for *New Horizons*' extended mission to another KBO (2014 MU₆₉).

why more craters on Pluto had a lower confidence than those on Charon (Fig. 4).

2. Different researchers mapping craters on lossless images generally found the same size-frequency distribution of data, though some found different spatial densities due to different thresholds of whether a feature is an impact crater. The 1σ spread in mapped crater diameter across all researchers and images on which craters were mapped averaged 10%·D, regardless of crater diameter. This natural variation should be carried through to other analyses as an uncertainty, such as to modeling the impactor population and using the data in scaling laws.

3. The global crater population of Pluto is extraordinarily non-uniform (also found by Stern et al., 2015; Moore et al., 2016), displaying some of the largest variations in the solar system. We only observe such extreme differences on Mars (north-south dichotomy and poles), Enceladus (South Pole versus the rest of the surface), and Ganymede (isolated areas show no craters in contrast with other heavily cratered regions).

4. The most densely cratered area of Pluto that we could map is just west of Sputnik Planitia. The peak $N(5)$ crater density, however, is only ≈60% that of the peak $N(5)$ crater density of Charon that we could map, and Charon's maximum $N(5)$ is only ∼35% the $N(5)$ of Nix after gravity scaling is accounted for. Therefore, the oldest surfaces on Nix and Hydra are the oldest we could measure in the system, and Charon's oldest surface is older than Pluto's oldest.

While individual impact craters and crater populations are used for a variety of scientific investigations, one of the main applications of craters is for modeling relative and absolute surface ages. The work presented in this paper demonstrates that there is variability in mapping impact craters based on available data and simple, inherent differences in individuals. If we were to use the range of crater densities found (Section 3.2), we would derive ages that vary by ±∼2×, and small deviations from a production function model might be interpreted as a resurfacing event as opposed to a single researcher's natural, stochastic variation. Consequently, this consensus dataset is likely to be the most robust for any set of solar system bodies, for it represents the use of multiple images, analysis by multiple researchers, and further verification of the combined results. We recommend its use in future crater-based investigations of Pluto, Charon, Nix, or Hydra, until future spacecraft can return further data. Specifically, we recommend that this database be used as a reference set for researchers wanting to do Pluto-Charon system crater research, either used in its entirety if the researcher is confident with our crater assessment, or as a cross-check to ensure the researcher has at least identified and measured the same high-confidence craters in this work. This database is available in the independent archive at http://astrogeology.usgs.gov/search/map/Pluto/Research/Craters/Craters_PlutoCharon_System_Robbins or, if USGS re-organizes their website, it will be available at the USGS's
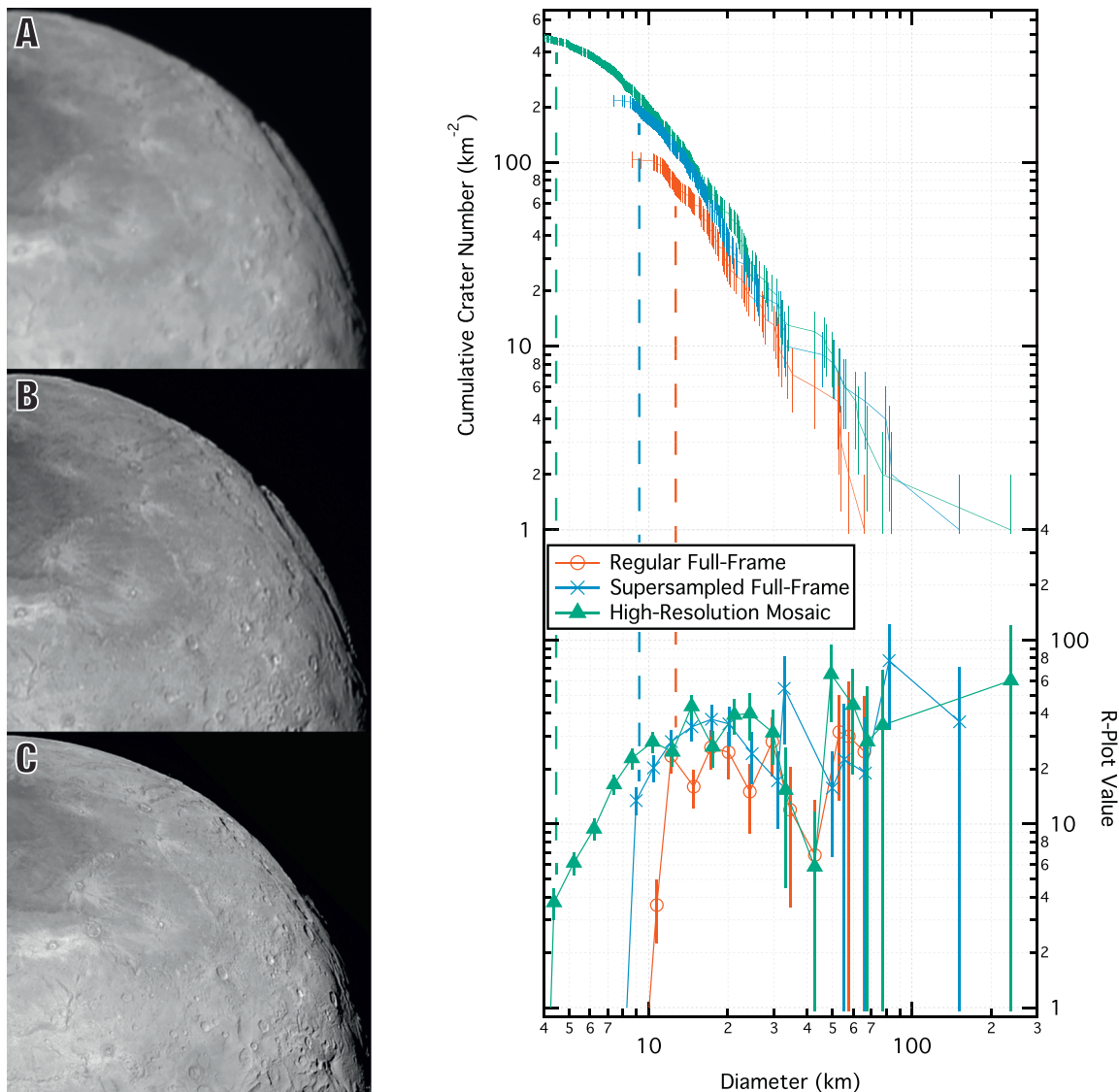
Fig. 14. Left column shows the same (or approximately same) quadrant of the encounter hemisphere of Charon where North is approximately up. Image A is a regular LORRI image from the last full-frame image before encounter (2.3 km/px), and image B shows a deconvolved version of the full-frame (∼1.2 km/px). Image C is a comparison from a higher resolution mosaic of Charon (∼0.9 km/px); note that the spacecraft had moved between these images and therefore C shows a slightly different part of the disk. The sub-spacecraft position was approximately 10°W, 40°N, and all craters within ∼25° of the limb were removed (craters > 18% of a Charonian circumference from the center of the disk). Robbins mapped impact craters on the full disk images of each of these and the SFDs of craters with confidence ≥ 3 are shown on the graph (see Fig. 1 caption for more detail about these plots, the caveat about area for the R plot values, and note there is no area normalization for cumulative crater number). When lower confidence craters are included, the supersampled image's data matches the high-resolution mosaic for $D \gtrsim 8$–9 km. The thick vertical, dashed lines indicate approximate completeness limits.

PDS Imaging and Cartography Node Annex, currently at http://astrogeology.usgs.gov/pds/annex.

Appendix A

Advanced image processing with supersampling and deconvolution

Completely apart from the artifacts generated by heavy compression, it must always be remembered that even a well-exposed, non-compressed image may be a poor or biased representation of the scene or object under study, especially as the resolution limit is approached. Both the sampling of an image with discrete pixels and the blurring by the point-spread function (PSF) will affect its representation of the fine scale information needed for accurate crater recognition and characterization of the most compact features. A primary goal of proper image processing is to understand the real object that is sampled by the image generated, free of all artifacts in the image-creation process. The Pluto Encounter team used a variety of techniques in an attempt to do this, and we "ground-truth" one of them below (and Fig. 14).

LORRI's PSF affects sampling at the scale of 2–3 pixels, and it has broad "wings" that can modestly blur features out to ∼dozen pixels (Cheng et al., 2008). This under-sampling causes aliasing which can both spuriously broaden or sharpen fine features similar in scale to the PSF, depending on their position with respect to the pixel array. In any extended object, it may do both, adding random

structural noise well above the nominal noise set by photon statistics. Fortunately, when an object is moved or "dithered" around the camera field from image to image in a sequence of exposures, all the relevant structural information admitted by the camera PSF may be contained in the full data set and can be used to synthesize a well-sampled, or "Nyquist image," that completely removes the deleterious effects of aliasing.

While most of the LORRI imaging provided only single exposures at a given location on Pluto or Charon, the highest resolution full-disk mosaics of both objects obtained a slightly-dithered pair of images at each position with only 1 sec between pairs. Further, given the modest degree by which the LORRI PSF is under-sampled, two dithers were typically sufficient to generate a Nyquist-sampled image. The image combination was done with the Fourier-based algorithm of Lauer (1999) which effectively interlaces a set of potentially non-optimally dithered images to generate a summed image with a finer pixel scale without introducing any additional blurring. The Lauer (1999) algorithm serves a similar image combination role to the well-known *Drizzle* algorithm, but *Drizzle* typically uses an interpolation kernel that adds significant blurring. In practice, the up-sampled LORRI images were produced with a scale twice as fine at the native LORRI sampling.

Coping with the effects of the PSF blurring on the crater detection is more complex. A standard option is to ignore it or simply cede the fine-scale information most strongly degraded by the PSF (i.e., assume the PSF blurring is significantly smaller than any feature that will be studied). Testing the effects of the PSF on simulated images is another approach (but requires significantly more work on the part of the crater analyst when the analyst does not know if the simulation and then image processing would be useful). As part of the analysis herein, deconvolution of the PSF was explored as a way to correct for the PSF independent of models or any assumed source properties.

Deconvolution was a controversial technique among many of the members of the *New Horizons* Pluto Encounter team. It can amplify random noise, and it can introduce artifacts (typically ringing at the edges of sharp, high-amplitude features in the image) that can be confused with real source structure – in particular, impact craters (e.g., Fig. 2C). Some of this concern is also set against a background of over-enthusiastic use of deconvolution without proper validation to inform its use in quantitative analysis (put colloquially in amateur terms, "sharpening like crazy"). Further, there is often a strong philosophy of avoiding image representations that are not easily traced back to the original pixel intensity measures. On the other hand, deconvolution has been increasingly recognized (based on increasing citation rates and usage) as a valuable research tool in astronomy since the advent of digital imagers with well-understood responses: when correctly applied, it can recover structural information in an image that can be exceedingly difficult to access by other methodologies. Simply stated, the best approach is to regard deconvolution as a potentially useful tool that can be used in parallel with other techniques and can be validated by simulations and cross checks.

Therefore, whether supersampling with deconvolution was useful in crater identification was examined with a full-disk LORRI image of Charon. Processing of the images was done with the Lucy-Richardson algorithm (Richardson, 1972; Lucy, 1974), which has a strong heritage of use with optical imagers, such as *Hubble Space Telescope* cameras. A crucial part of the deconvolution is accurate knowledge of the PSF, which for LORRI was provided by rich observations of open star clusters during the cruise phase of the mission. In short, Nyquist-sampled PSFs were constructed (using the Lauer (1999) algorithm) over a grid of locations in the LORRI field to account for small spatially-dependent variations in the PSF. The deconvolution procedure was to break any image into smaller areas using the PSF appropriate to a given section. Deconvolution

works best on Nyquist-sampled images, but it is still effective on under-sampled images. LORRI PSFs, constructed with 2×2 supersampling, were down-sampled to the native LORRI resolution.

Only the full disk image of Charon was examined for supersampled-deconvolution effects (Fig. 14). Based on comparisons of craters with confidence ≥ 3, shown in Fig. 14, the Charon full-frame image yielded similar results to the higher-resolution mosaic for $17 \lesssim D \lesssim 60$ km, corresponding to craters as small as 7.3 pixels on the original full-disk image. The super-sampled version matches $11 \lesssim D \lesssim 200$ km (≈ 4.8 px on the original image). Not shown is the comparison that includes all craters regardless of confidence, where the SFDs match to $D \gtrsim 8$–9 km, a mere 3.5–4.0 px on the original full-frame image. Put another way, using images that originally had a pixel scale of the full-frame image (2.3 km/px, shown in red in Fig. 14 (color refers to electronic version)), we were able to reproduce the crater population for the same region to a pixel size as small as 4.8 px on the original; and, when just analyzing the original image (2.3 km/px), the population that was observed had as few as 30% less craters at any given diameter and only produced the same SFD slope/shape (when "ground-truthed" against the higher resolution mosaic) for craters > 7.4 px (> 17 km).

Many crater analysts will anecdotally state that craters $D \lesssim 8$ px are unreliable both in number and diameter, and this was quantified in Robbins et al. (2014) where they demonstrated significant – and different – artifacts on a per-analyst basis for craters $D \lesssim 10$ px. Being able to reliably push crater identification to the $D \approx 5$–7 px level would significantly improve the ability to use spacecraft imagery for crater-based studies (increasing the potential number of craters by $\sim$2–8$\times$). However, it should be noted that there are some crater analysts who are comfortable with craters as small as $D \approx 5$–8 px without any special image processing; this is an area without consensus in the cratering community.

The analysis in this section demonstrates this supersampling-deconvolution process can yield images that are reliable for mapping small impact craters that otherwise would not be identifiable. However, future analysts will need to make their own decision about whether they will trust features that cannot be validated with higher-resolution, non-existent imagery.

References

Aban, I.B., Meerschaert, M.M., Panorska, A.K., 2006. Parameter estimation for the truncated pareto distribution. J. Am. Stat. Assoc. 101, 270–277. http://dx.doi.org/10.1198/016214505000000411.

Beyer, R.A., et al., 2017. Charon tectonics. in rev. Icarus.

Bierhaus, E.B., Dones, L., 2015. Craters and ejecta on Pluto and Charon: Anticipated results from the *New Horizons* flyby. Icarus 246, 165–182. http://dx.doi.org/10.1016/j.icarus.2014.05.044.

Buie, M.W., Grundy, W.M., Young, E.F., Young, L.A., Stern, S.A., 2010. Pluto and Charon with the *Hubble Space Telescope*. II. Resolving changes on Pluto's surface and a map for Charon. Astronom. J. 139, 1128–1143. http://dx.doi.org/10.1088/0004-6256/139/3/1128.

Cheng, A.F. and 15 co-authors, 2008. Long-Range Reconnaissance Imager on New Horizons. Space Sci. Rev. 140, 189–215. http://dx.doi.org/10.1007/s11214-007-9271-6.

Ester, M., Kriegel, H.-P., Sander, J., Xu, X., 1996. A density-based algorithm for discovering clusters in large spatial databases with noise. In: Proceedings of the 2nd International Conference on Knowledge Discovery and Data Mining. AAAI Press, pp. 226–231. ISBN 1-57735-004-9.

Gault, D.E., 1970. Saturation and equilibrium conditions for impact cratering on the lunar surface: Criteria and implications. Radio Sci 5, 273–291. http://dx.doi.org/10.1029/RS005i002p00273.

Greenstreet, S., Gladman, B., McKinnon, W.B., 2015. Impact and cratering rates on Pluto. Icarus 258, 267–288. http://dx.doi.org/10.1016/j.icarus.2015.05.026.

Klaasen, K.P. and 15 co-authors, 1997. Inflight performance characteristics, calibration, and utilization of the *Galileo* solid-state imaging camera. Opt. Eng. 36:11, 3001–3027. http://dx.doi.org/10.1117/1.601525.

Klaasen, K.P. and 11 co-authors, 1999. Calibration and performance of the *Galileo* solid-state imaging system in Jupiter orbit. Opt. Eng. 38:7, 1178–1199. http://dx.doi.org/10.1117/1.602168.

Lauer, T.R., 1999. Combining undersampled dithered images. PASP 111, 227–237. http://dx.doi.org/10.1086/316319.

Lucy, L.B., 1974. An iterative technique for the rectification of observed distributions. Astronom. J. 79:4, 745–754. http://dx.doi.org/10.1086/111605.

Hiesinger, H. and 22 co-authors, 2016. Cratering on Ceres: implications for its crust and evolution. Science 353, 1003–1011. http://dx.doi.org/10.1126/science.aaf4759.

Holsapple, K.A., 1993. The scaling of impact processes in planetary sciences. Ann. Rev. Earth Planet. Sci. 21, 333–373. http://dx.doi.org/10.1146/annurev.ea.21.050193.002001.

Marchi, S. and 11 co-authors, 2012. The violent collisional history of asteroid 4 Vesta. Science 336 (6082), 690–694. http://dx.doi.org/10.1126/science.1218757.

Marchi, S., Bottke, W.F., O'Brien, D.P., Schenk, P., Mottola, S., De Sanctis, M.C., Kring, D.A., Williams, D.A., Raymond, C.A., Russell, C.T., 2013. Small crater populations on Vesta. Planet. & Space Sci. 103, 96–103. http://dx.doi.org/10.1016/j.pss.2013.05.005.

Mick, A., Firer, J., Bogdanski, J., Williams, S., Birrane, E., Krupiarz, C., 2008. *New Horizons* solid-state recorder electronics and open-source software. Space Technology 28, 19–32.

Moore, J.M. and 40 co-authors, 2016. The geology of Pluto and Charon through the eyes of New Horizons. Science 351:6279, 1284–1293. http://dx.doi.org/10.1126/science.aad7055.

O'Brien, D.P., Marchi, S., Morbidelli, A., Bottke, W.F., Schenk, P.M., Russell, C.T., Raymond, C.A., 2014. Constraining the cratering chronology of Vesta. Planet. & Space Sci. 103, 131–142. http://dx.doi.org/10.1016/j.pss.2014.05.013.

Porter, S.B., et al., 2016. The small satellites of Pluto. Lunar & Planet. Sci. Conf. 47, Abstract #2016.

Reuter, D.S. and 19 co-authors, 2008. Ralph: A visible/infrared imager for the New Horizons Pluto/Kuiper belt mission. Space Sci. Rev. 140, 129–154. http://dx.doi.org/10.1007/s11214-008-9375-7.

Richardson, W.H., 1972. Bayesian-based iterative method of image restoration. J. Optical Soc. Amer. 62, 55–59.

Robbins, S.J. and 10 co-authors, 2014. The variability of crater identification among expert and community crater analysts. Icarus 234, 109–131. http://dx.doi.org/10.1016/j.icarus.2014.02.022.

Robbins, S.J. and 24 co-authors, 2016. Geologic map of *New Horizons*' encounter hemisphere of Charon. Planet. Mappers Mtg., Abstract #7026.

Schenk, P.S., Marchi, S., O'Brien, D.P., Russell, C.T., Raymond, C.A., 2015. Morphology and age of Rheasilvia (Vesta), and expectations for large impact basins on Ceres. Lunar & Planet. Sci. Conf. 46, Abstract #2309.

Schmedemann, N. and 13 co-authors, 2013. Lunar-Like chronology for Vesta – Crater Retention ages matching independent Ar-Ar HED ages. Lunar & Planet. Sci. Conf. 44, Abstract #2155.

Schmedemann, N. and 18 co-authors, 2014. The cratering record, chronology and surface ages of (4) Vesta in comparison to smaller asteroids and the ages of HED meteorites. Planet & Space Sci 103, 104–130. http://dx.doi.org/10.1016/j.pss.2014.04.004.

Showalter, M.R., Hamilton, D.P., 2015. Resonant interactions and chaotic rotation of Pluto's small moons. Nature 522, 45–49. http://dx.doi.org/10.1038/nature14469.

Stern, S.A. and 150 co-authors, 2015. The Pluto system: Initial results from its exploration by New Horizons. Science 350 (6258). http://dx.doi.org/10.1126/science.aad1815.

Weaver, H.A. and 50 co-authors, 2016. The small satellites of Pluto as observed by New Horizons. Science 351:6279. http://dx.doi.org/10.1126/science.aae0030.

White, O.L., Stern, S.A., Weaver, H.A., Olkin, C.B., Ennico, K., Young, L.A., Moore, J.M., Cheng, A.F. and the New Horizons Geology, Geophysics, and Imaging Theme Team, 2016. Geological mapping of the encounter hemisphere on Pluto. Lunar & Planet. Sci. Conf. 47, Abstract #2479.